University of Nevada, Reno

Deep Learning Approach to Improve Spatial Resolution of GOES-17 Wildfire Boundaries using VIIRS Satellite Data

A thesis submitted in partial fulfillment of the

requirements for the degree of Master of Science in

Computer Science and Engineering

by

Mukul Badhan

Dr. Hamed Ebrahimian and Dr. George Bebis - Thesis Advisors

May, 2023

THE GRADUATE SCHOOL

We recommend that the thesis
prepared under our supervision by

Mukul Badhan

entitled

Deep Learning Approach to Improve Spatial Resolution of GOES-17 Wildfire Boundaries using VIIRS Satellite Data

be accepted in partial fulfillment of the
requirements for the degree of

MASTER OF SCIENCE

Hamed Ebrahimian, Ph.D.

Advisor

George Bebis, Ph.D.

Co-advisor

Mircea Nicolescu, Ph.D.

Committee Member

Neil P. Lareau, Ph.D.

Graduate School Representative

Markus Kemmelmeier, Ph.D., Dean

Graduate School

May 2023

Abstract

The rising severity and frequency of wildfires in recent years in the U.S. have raised numerous concerns regarding the improvement in wildfire emergency response management and decision-making systems, which require operational high temporal and spatial resolution monitoring capabilities. Satellites are one of the tools that can be used for wildfire monitoring. However, none of the currently available satellites provide both high temporal and spatial resolution. For example, GOES-17 geostationary satellite has a high temporal (5 min) but a low spatial resolution (2 km), and VIIRS polar orbiter satellite has a low temporal (~12 h) but high spatial resolution (375 m). This study aims to leverage currently available satellite data sources, such as GOES and VIIRS, along with Deep Learning (DL) advances to achieve an operational high-resolution wildfire monitoring tool.

This study considers the problem of increasing the spatial resolution of low resolution satellite data using high resolution satellite. An Autoencoder DL model is proposed to learn how to map GOES-17 geostationary low spatial resolution satellite images to VIIRS polar orbiter high spatial resolution satellite images. In this context, several loss functions and architectures are implemented and tested to predict both the area of fire and corresponding fire radiance values. These models are trained and tested on wildfire sites from 2019 to 2021 in the western U.S. The results indicate that DL models can improve the spatial resolution of GOES-17 images, leading to images that mimic the spatial resolution of VIIRS images. Combined with GOES-17 higher temporal resolution, the

DL model can provide high-resolution near-real-time wildfire monitoring capability as well as semi-continuous wildfire progression maps.

Acknowledgments

I wish to thank my advisor, Dr. Hamed Ebrahimian, co-advisor Dr. George Bebis, Dr. Neil P. Lareau, and my mentor and friend, Kasra Shamsaei, for their support throughout this process. This material is based upon work supported by the NSF-LEAP-HI program under grant number CMMI-1953333 with Dr. Hamed Ebrahimian as the PI.

The content of this thesis and mainly Chapter 2 is currently being prepared for submission for publication of the material by Mukul Badhan, Kasra Shamsaei, Dr. Hamed Ebrahimian, Dr. George Bebis, Dr. Neil P. Lareau. The thesis author is the primary investigator and author of the work. The work will be published with a title that closely resembles the title of this thesis.

Contents

List of Tables

List of Figures

Chapter 1: Introduction

In recent years, United States has experienced an alarming increase in the number and severity of wildfires. The National Interagency Fire Center reports that since the 1980s, the number of acres burned by wildfires has been steadily increasing, with a peak in 2015 of over 10 million acres burned across the country [1]. The western United States, especially California, has experienced severe impacts from these devastating fires. One example is the Dixie Fire, which burned from July 14 to November 9, 2021. It ravaged over 960,000 acres, destroyed more than 1,300 structures, and resulted in a firefighter and a civilian causality, with several injuries reported. The estimated cost of Dixie Fire is over $637 million [2]. Another instance is the Caldor Fire, which burned from August 14 to September 22, 2021, consuming over 220,000 acres and destroying more than 1,000 structures. Moreover, two firefighters and one civilian lost their lives, and several others were injured. The cost of Caldor Fire was estimated at over $271 million [3]. Climate change, anthropogenic activities, and other factors have exacerbated the frequency and severity of wildfires in recent years [4]. Catastrophic wildfire events have significant Short- and long-term direct and indirect impacts on social system, economy, human health, ecosystem, watersheds, and built environment. Hence, the need for effective wildfire monitoring has become more pressing than ever. Real-time monitoring is crucial for providing timely and accurate information on the location, size, and intensity of wildfires. This data is essential for effective emergency response management efforts and for making decisions related to firefighting, public safety, and evacuation orders. Automated monitoring systems that can provide real-time data on wildfires can

significantly reduce the risks faced by firefighters, enabling them to respond quickly and safely.

Remote sensing provides information such as the location of active fires, rate of spread, and radiated energy which can help to analyze wildfire behavior and mitigate its impact [5]. Several fire detection and monitoring systems have been developed using remote sensing technologies, mainly terrestrial-based systems, aerial-based systems, and satellite-based systems [6]. Terrestrial-based systems are generally considered to be more efficient than other systems in terms of accuracy and response time to wildfire incidents, owing to their high-resolution cameras/sensors, appropriate viewing angles, and proximity to wildfire sites. However, their coverage is limited compared to other solutions due to their fixed positions, and they are vulnerable to occlusions [7]. Aerial-based systems typically provide enough resolution to achieve detailed fire progression mapping, but their deployment during an emergency may not always be possible due to safety and financial constraints. Additionally, they encounter problems such as temporal and data processing inconsistency due to the broad range of sensors used for this purpose [8][9]. In contrast, the Earth Observation (EO) satellite system monitors fire activity by utilizing algorithms that detect the location of fires actively burning at the time of satellite overpass over a vast area. This allows the system to quickly detect and identify the location of wildfires, even in remote or inaccessible areas. The captured raw data is validated to create reliable and consistent data [10]. Despite the many advantages of the EO satellite system, it has some limitations compared to other wildfire monitoring systems. The spatial and/or temporal resolution of these systems are restricted, which means that it may not provide the level of detail needed for emergency response

applications. The EO system employs various types of satellites, including those in Low Earth Orbits (LEO) and Geosynchronous Equatorial Orbits (GEO). LEO satellites fly closer to Earth and provide high spatial resolution but typically capture snapshots of the same area at large temporal frequency (e.g., hours of days) [11]. Some examples of LEO satellites are Landsat-8/9 and Sentinel-2A/2B sensors, which offer 10 m to 30 m multi-spectral global coverage [12]. Although satellite images from Sentinel-2 [13] and Landsat-8 [14][13] have been used for active fire detection, the revisit interval of 5 days for Sentinel-2 and 8 days for Landsat-8/-9 is infrequent to detect active fires reliably [15]. Several instruments on board LEO satellites, including the Visible Infrared Imaging Radiometer Suite (VIIRS) [16] on the Suomi National Polar-orbiting Partnership (NPP) satellite, Sea and Land Surface Temperature Radiometer (SLSTR) on the Sentinel-3 satellite, and the Moderate Resolution Imaging Spectroradiometer (MODIS) [17] on the Terra and Aqua satellites, are commonly used to detect active fire points. These sun-synchronous orbit satellites provide coarse-resolution data using the medium infrared (MIR) band, with twice-daily revisits. Active fire products have been developed using these LEO satellites to provide the location and time of active fires on a daily basis [18]. For instance, VIIRS offers a 375 m spatial resolution, while MODIS offers a 1 km spatial resolution [19][20]. The high spatial resolution of the VIIRS sensor helps detect more active fire pixels, as it can detect low-intensity fires [21]. Sentinel-3 SLSTR has a similar capture time and spatial resolution as MODIS but can detect fires with lower fire radiance power (FRP) [22] than MODIS [18]. On the other hand, GEO sensors provide high temporal resolution but lower spatial resolution (2 km) than the previous category due to their higher elevation from the Earth [23]. An example of a GEO satellite is the

Geostationary Operational Environmental Satellites R Series (GOES-R), which consists of two geostationary satellites, GOES-16 and GOES-17, that have constant watch over the whole western hemisphere, including North America, South America, the Pacific Ocean, the Atlantic Ocean, and Western Africa. However, the GOES-R active fire product has been found to be not adequately reliable, with a false alarm rate of around 60% to 80% for medium and low confidence fire pixels [24].

Given the limitations of both GEO and LEO satellites, a non-physical remote sensing tool based on Artificial Intelligence (AI) has the potential to improve temporal and spatial accuracy in monitoring wildfires. AI, specifically DL , has been effective in solving complex tasks like image classification [25], object detection [26][27], and semantic segmentation [28]. Building on these successes, recent research has explored the use of DL methods on satellite imagery for tasks such as land-use classification, including the extraction of building [29], and urban planning [30][31]. By leveraging AI principles such as image segmentation and super-resolution, it may be possible to develop a highly accurate wildfire prediction system that can improve our ability to detect and respond to wildfire incidents.

Few recent studies have proposed DL-based approaches for early wildfire detection from streams of remote sensing data. These studies have focused mainly on detecting the presence of fire without predicting its intensity. Toan et al. (2019) propose a deep convolutional neural network (CNN) architecture for classifying hyperspectral satellite images as containing wildfire or not [32]. The study proposes a deep CNN architecture that uses patch normalization to augment the training data and reduce the complexity of

fully connected networks using a fully connected network at the end. The network is trained on a dataset of hyperspectral satellite images (GOES) to classify each pixel as either containing wildfire or not. The study demonstrates the potential of using DL methods for early wildfire detection and monitoring. In a related study, Toan et al. (2020) propose another DL-based approach for the early detection of bushfires using multi-modal remote sensing data [33]. The proposed approach consists of a DL model that incorporates both CNNs and long short-term memory (LSTM) networks. The model is designed to process multi-modal remote sensing data at different scales, ranging from individual pixels (using CNN) to entire images (using LSTM). The authors report a high level of accuracy in detecting outperforming several other state-of-the-art methods. Zhao et al. (2022) focuses on the use of time-series data from the GOES-R for early detection of wildfires [34]. The study proposes a DL model that incorporates a gated recurrent unit (GRU) network to process the time-series data from GOES-R. The model is designed to learn the spatio-temporal patterns of wildfire events and predict their likelihood at different locations. The authors also use a sliding window technique to capture the temporal dynamics of wildfire events. The authors demonstrate that the model can detect wildfire events several hours before they are reported by official sources. Finally, McCarthy et al. (2021) proposes an extension of U-Net CNNs to geostationary remote sensing imagery to improve the spatial resolution of active wildfire detections and enable high-resolution active wildfire monitoring from space [35]. The study leverages the complementary properties of GEO and LEO sensors and static features related to topography and vegetation to inform the analysis of remote sensing imagery with physical knowledge about fire behavior. However, the study acknowledges a limitation of

the proposed algorithm in terms of false positives and emphasizes the need for further research to address this issue. Overall, the four papers reviewed demonstrate the potential of DL methods in the early detection and monitoring of wildfires using remote sensing data from different sources. They provide insights regarding different approaches that can be used to improve the accuracy and efficiency of wildfire detection and monitoring, which have practical implications for decision support during rapidly unfolding wildfires. However, these works are limited in terms of the number of wildfire events studied and are also limited to just detecting the fire and not its intensity. To the best of our knowledge, there is no published study that improves the spatial resolution of GOES while also predicting fire intensity values.

This study aims to address the gap in wildfire monitoring and mitigation by presenting a framework that utilizes DL techniques to enhance the spatial resolution of GOES-17 satellite images using VIIRS data. The main objective is to determine the optimal solution by conducting an ablation study on four cases, using different loss functions and variations in autoencoder architecture. To enable DL models to use contemporaneous data that share similar spectral and projection characteristics, a scalable dataset creation pipeline is developed, which can accommodate the addition of new sites. This study also addresses the challenges of selecting an appropriate evaluation metric to determine the optimal solution. Additionally, the proposed system includes a novel streaming data feature that can enable proactive monitoring, identification, and reaction to wildfires by experts. An automated real-time streaming and visualization dashboard system can utilize the proposed framework, which will transform relevant GOES data for the selected location into high-resolution images with both high spatial resolution and near-real-time

accuracy. The thesis is structured as follows: Chapter 2 provides detailed research information. Section 1 of Chapter 2 presents an overview of the satellite used in the study and describes the preprocessing steps taken to ensure consistency. Section 2 of Chapter 2 discusses the model setup, including the autoencoder, loss functions, and evaluation metrics used in the study. Finally, Section 3 of Chapter 2 presents the results with empirical evaluations. The thesis concludes with Chapter 3.

Chapter 2: Research Details

1. Methodology

1.1. Data Source

1.1.1. Geostationary Operational Environmental Satellite (GOES)

Launched by the National Oceanic and Atmospheric Administration (NOAA), GOES-17 is operational as GOES-West since February 12, 2019. This Geostationary satellite is 35,700 km above earth providing constant watch over the pacific ocean and the western United States [36]. The Advanced Baseline Imager (ABI) is the primary instrument of the GOES for imaging Earth's weather, oceans, and environment. ABI views the Earth with 16 spectral bands, including two visible channels (channels 1-2 with approximate center wavelengths of 0.47 and 0.64 μm), four near-infrared channels (channels 3-6 with approximate center wavelengths of 0.865, 1.378, 1.61, and 2.25 μm), and ten mid- and long-wave infrared (IR) channels (channels 7-16 with approximate center wavelengths 3.900, 6.185, 6.950, 7.340, 8.500, 9.610, 10.350, 11.200, 12.300, and 13.300 μm) [36]. These channels are used by various models and tools to monitor different elements on the earth's surface, such as trees and water, or in the atmosphere, such as clouds, moisture, and smoke [36]. Dedicated products are available for cloud formation, atmospheric motion, convection, land surface temperature, ocean dynamics, vegetation health, and flow of water, fire, smoke, volcanic ash plumes, aerosols, air quality, etc. [37].

In this study, channel 7 (IR shortwave) of Level 1B (L1B) Radiances product (ABI-L1b-Rad) is used as input for DL model of this study. The product, with its scan mode six, captures one observation every 5 min of the Continental U.S. (CONUS) with a spatial

resolution of 2 km [38]. The L1B data product contains measurements of the radiance values (measured in milliwatts per square meter per steradian per reciprocal centimeter) from the Earth's surface and atmosphere. These radiances are used to identify cloudy and hot regions within the satellite's field of view [39].

1.1.2. Visible Infrared Imaging Radiometer Suite (VIIRS)

The Visible Infrared Imaging Radiometer Suite (VIIRS) instrument is installed on two polar orbiter satellites, namely Suomi National Polar-orbiting Partnership (S-NPP) operational from 7 March, 2012 [40] and NOAA's Joint Polar Satellite System (JPSS), now called NOAA-20, operational from 7 March, 2018 [41]. These two satellites are 50 min apart, 833 km above the earth, and revolve around the earth in a polar orbit [41]. For each site, these satellites make two passes daily - one during the day and one at night [42]. VIIRS features daily imaging capabilities across multiple electromagnetic spectrum bands to collect high-resolution atmospheric imagery including visible and infrared images to detect fire, smoke, and particles in the atmosphere [43]. The VIIRS instrument provides 22 spectral bands, including five imagery 375 m resolution bands (I bands), 16 moderate 750 m resolution bands (M bands), and one Day-Night Band (DNB band) [44]. The I bands include a visible channel (I1), a near-IR (I2), a shortwave IR (I3), a mediumwave IR (I4), and a longwave IR (I5) with center wavelengths of 0.640, 0.865, 1.610, 3.740, and 11.450 μm, respectively. The M bands include five visible channels (M1-M5), two near IR channels (M6-M7), four shortwave IR channels (M8-M11), two mediumwave IR channels (M12-M13), and three longwave IR channels (M14-M16) with center wavelengths of 0.415, 0.445, 0.490, 0.555, 0.673, 0.746, 0.865, 1.240, 1.378, 1.610, 2.250, 3.700, 4.050, 8.550, 10.763, and 12.013 μm, respectively [44]. VIIRS also

hosts a unique panchromatic Day/Night band (DNB), which is ultra-sensitive in low-light conditions and is operated on central wavelength of 0.7 μm [45] .

In this study, VIIRS (S-NPP) I Band Active Fire Near-Real-Time product with 375 m resolution, i.e., VNP14IMGTDL_NRT, [46] is used as ground truth to improve the spatial resolution of GOES imagery due to its relatively high spatial resolution compared to GOES (375 m vs. 2 km). The product's data are available from January 20, 2012 to present [47]. VIIRS shows good agreement with its predecessors in hotspot detection [48], and it provides an improvement in the detection of relatively small fires as well as the mapping of large fire perimeters [49].

1.2. Data Pre-Processing

DL models require two sets of images: input images (i.e., GOES images herein) and ground truth or reference images (i.e., VIIRS images herein). The prediction of DL model and ground truth are compared pixel-by-pixel, and the difference between the prediction and ground truth (i.e., loss function value) is used by the model to learn its parameters via backpropagation. Hence, the input and ground truth should have the same size, projection, time instance, and location. However, the initial format of GOES and VIIRS data are different. The VIIRS has vector data in CSV format [38][50] whereas the GOES data are raster data in NetCDF format [51][52]. They differ in the way they represent geographic features; vector data represents features as points or lines, while raster data represents them as pixels arranged in a grid. Additionally, vector data needs to be converted into a pixel-based format, while raster data are already in the correct format for display [53]. Furthermore, GOES images contain a snapshot of both fire and background

information, whereas VIIRS's CSVs contain the location and radiance value of globally detected fire hotspots. Therefore, data pre-processing is required to make the initial formats and projections of these data consistent.

The pre-processing pipeline aims to create a consistent dataset of images from multiple wildfire sites, with standardized dimensions, projections, and formats. Each processed GOES image in the dataset will correspond to a processed VIIRS image representing the same region and time instance of a wildfire event. To facilitate this process, a comprehensive list of wildfire events in the western U.S. between 2019 and 2021 is compiled from multiple sources [54][55] (see Appendix A). This wildfire property list (WPL) plays a crucial role in several pre-processing steps, such as defining the region of interest (ROI) for each wildfire site. To obtain the four corners of the ROI, a constant value is added/subtracted from the central coordinates specified in the WPL. For each wildfire event defined by its ROI and duration mentioned in the WPL, the pre-processing pipeline conducts the following four steps.

- Step 1: *Extracting wildfire event data from VIIRS and identifying timestamps.* The pipeline first extracts the records from the VIIRS CSV to include fire hotspots that fall within the ROI and duration of wildfire event. The pipeline also identifies unique timestamps from the extracted records.
- Step 2: *Downloading GOES images for each identified timestamp.* In order to ensure a contemporaneous dataset, the pre-processing pipeline downloads GOES images with captured times that are near to each VIIRS timestamp identified in Step 1. GOES have a temporal resolution of 5 minutes, meaning that there will

always be a GOES image within 2.5 minutes of the VIIRS capture time, except in cases where the GOES file is corrupted [56]. It should be noted that Steps 3 and 4 are halted if the respective GOES file is corrupted.

- Step 3: *Creating processed GOES images.* The GOES images obtained in Step 2 cover the western U.S. and Pacific Ocean and have a projection different from VIIRS. In this step, the GOES images are cropped to match the site's ROI and reprojected into a standard coordinate reference system (CRS).
- Step 4: *Creating processed VIIRS images.* The VIIRS records obtained in Step 1 are grouped by timestamp and rasterized, interpolated, and saved into GeoTIFF images using the same projection as the one used to reproject GOES images in Step 3.

These steps are explained in more detail in the following subsections. Once these steps are completed, the GOES and VIIRS images will have the same image size and projection. An example of the processed GOES and VIIRS images is shown in Figure 1a and 1b, respectively. In Figure 1c, where the VIIRS image is overlaid on the GOES image, the VIIRS fire region almost completely covers the GOES fire region, which verifies the data pre-processing pipeline. It should be noted that in Figure 1a, the GOES image includes both fire pixels and background information, while in Figure 1b, the output VIIRS image only contains fire pixels and no background information.

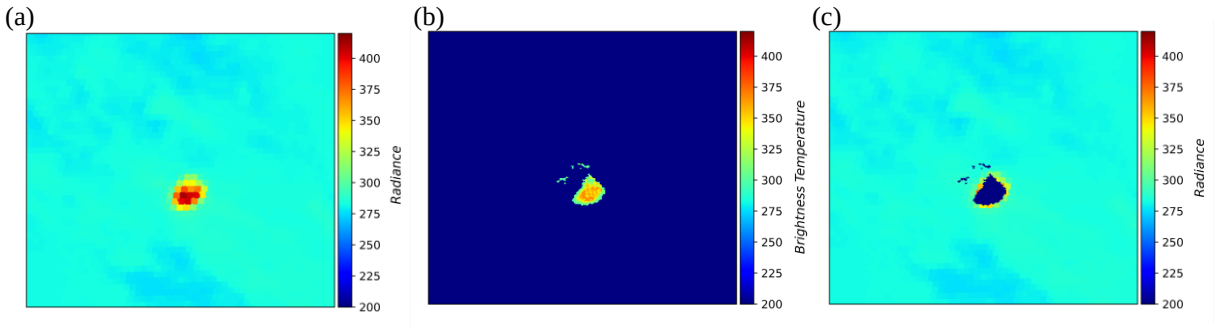

Figure 1: An illustration of data pre-processing outcomes for Kincade fire site at 2019-10-27 9:49 UTC (a) processed GOES image, (b) processed VIIRS image, (c) overlapped GOES and VIIRS images, where radiance's units are $\frac{mW}{m^2 sr(cm^{-1})}$ *and brightness temperature's units are K.*

1.2.1. GOES Pre-Processing

The NOAA Comprehensive Large Array-data Stewardship System (CLASS) repository [3] is the official site for accessing GOES products. ABI fire products are also available publicly in Amazon Web Services (AWS) S3 Buckets [4]. The Python s3fs [5] library, which is a filesystem in user space (FUSE) that allows mounting an AWS S3 bucket as a local filesystem, is utilized in this study to access the AWS bucket "NOAA-GOES17".

As previously mentioned, the downloaded GOES images cover the western U.S. and Pacific Ocean, and need to be cropped to the specific wildfire site's ROI. Additionally, the unique projection system of GOES, known as the "GOES Imager Projection" [57] must be transformed to the standard CRS to make it comparable with VIIRS. For this study WGS84 system (latitude/longitude) is used as the standard CRS. The projection conversion is achieved using Satpy python library [58], which is specifically designed for reading, manipulating, and writing data from earth-observing remote sensing instruments. Specifically, the Satpy scene function [59] is utilized to create a GOES scene from the downloaded GOES file, which allows the transformation of the GOES CRS to the

WGS84 system [60]. The Satpy area definition [61] is then applied to crop the GOES scene to match the ROI.

1.2.2. VIIRS Pre-Processing

Annual summaries of VIIRS-detected fire hotspots in CSV format, are accessible by country through the Fire Information for Resource Management System (FIRMS) [51], which is a part of NASA's Land Atmosphere Near-Real-time Capability for Earth Observing System (LANCE) [52]. In this study, annual summaries from 2019 to 2021 are utilized since corresponding GOES-17 files are only available from 2019. The CSVs contain the I-4 channel brightness temperature (3.55-3.93 μm) of the fire pixel measured in K, referred to as b-temperature I-4, along with the acquisition date, acquisition time, and latitude and longitude fields. Notably, the annual summary files are exclusively available for S-NNP.

The VIIRS-detected fire hotspot vector data are available in CSV format, with each record containing details about the intensity of a fire hotspot and other relevant information (satellite name, day-night flag, etc.) at a specific time and location. The longitude and latitude coordinates of each fire hotspot define its location at the center of a 375 by 375 m pixel. To ensure its compatibility with GOES data for the DL model, the vector data is converted into a pixel-based format through rasterization [62]. This process involves mapping the vector data to pixels, resulting in an image that can be displayed [63]. This process involves three main steps: defining the ROI, defining the grid system over the ROI, and mapping the fire data to the pixels. The process is illustrated schematically in Figure 2.

The first step involves defining the ROI for the wildfire site. To accomplish this, a constant value C = 0.6 degrees is added/subtracted from the center coordinates of the fire site, as defined in the WPL, to obtain the four corners of the ROI. Figure 2a shows the defined ROI around the center of fire hotspot represented by the red dots. The second step is to overlay grid system over the ROI. Each cell in the grid system corresponds to a single pixel in the output image, and a specific cell size of 375 by 375 m is selected to match the resolution of the VIIRS hotspot detection. The process involves transforming the entire ROI from longitude/latitude (degree) space to northing/easting or distance space, using PyProj's transformation function [64]. Once the ROI is in the distance space, it can be segmented into cells of the desired size, thereby creating a grid system with the required resolution, as illustrated in Figure 2b. The final step is to map the fire locations from the CSV file to the corresponding pixels. If the central coordinates of fire hotspot fall within a cell associated with a pixel, that pixel is activated and assigned a value based on the b-temperature I-4 value from VIIRS CSV. Figure 2c illustrates this process by showing the activation of pixels without displaying their actual values, for simplicity.

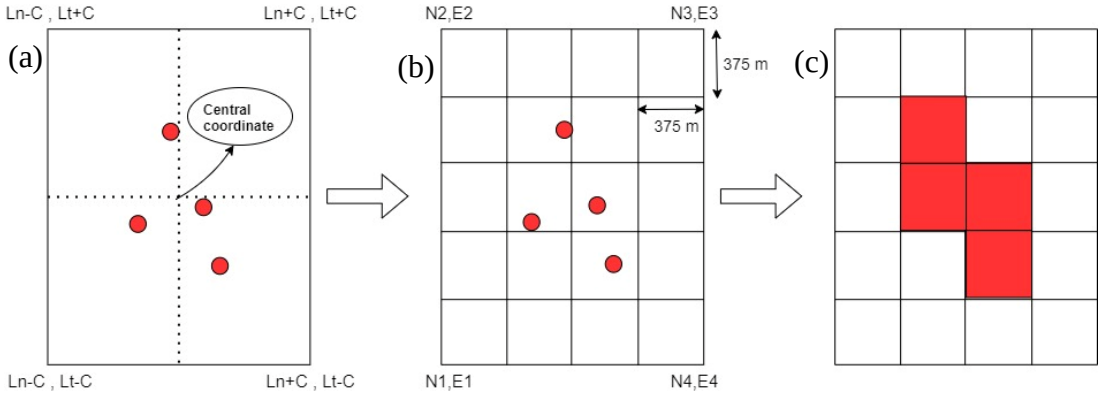

Figure 2: VIIRS data rasterization process, (a) region of interest in longitude/latitude (Ln, Lt) space, (b) grid over region of interest in Northing/Easting space, and (c) output image.

Following the rasterization process, nearest neighbor interpolation [65] is performed for non-fire pixel with neighboring fire pixel. This interpolation method is used to eliminate any artificial patches in and around the fire region, as shown in Figure 3a, and to ensure that the output image, as shown in Figure 3b, accurately represents the extent and intensity of the wildfire. Finally, the created raster is saved in GeoTIFF format using the GDAL library [66].

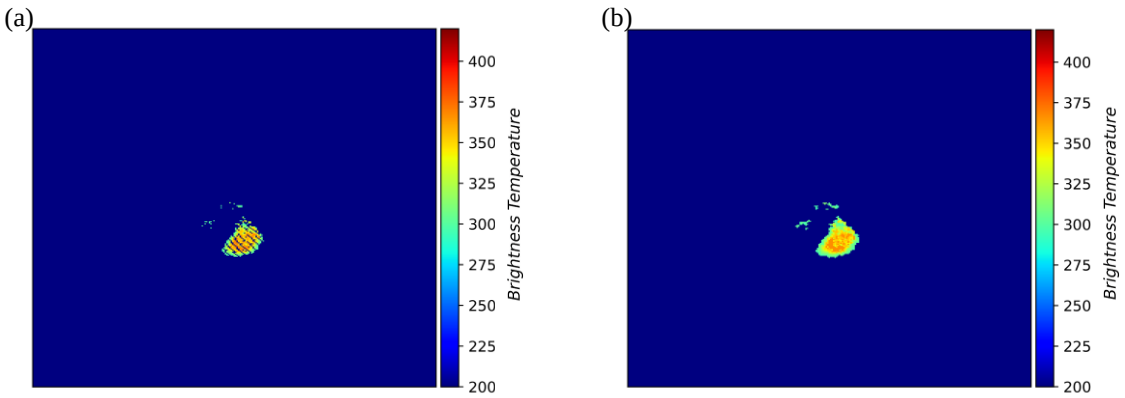

Figure 3: VIIRS data interpolation process (a) pre-interpolation VIIRS output, (b) post-interpolation VIIRS output, where brightness temperature's units are K.

2. Model Setup

2.1. Autoencoder

Autoencoder is a popular DL architecture for image super-resolution [67]. It takes the low-resolution image as input, learns to recognize the underlying structure and patterns, and generates a high-resolution image that closely resembles the ground truth [68]. Autoencoder has two main components: the encoder, which extracts important features from the input data, and the decoder, which generates an output based on the learned features. Together, they effectively distill relevant information from input and reproduce it as output [68].

In this study, an autoencoder was tasked with distilling the relevant portions of the input GOES-17 imagery to reproduce an output with increased resolution and removed background noise (such as reflections from clouds, lakes, etc.) to mimic VIIRS imagery. The model's encoder component is composed of five two-dimensional convolutional layers with a kernel size of three and a padding of one, followed by a Rectified Linear Unit (ReLu) activation layer [69]. This architecture allows the model to recognize important features in the low-resolution input images while preserving their spatial information. The use of ReLu activation layers after each convolutional layer helps to introduce non-linearity, which is critical for the network's ability to learn complex patterns in the input images. Additionally, the second and fourth convolutional layers are followed by max pool layers, which help to down-sample the feature maps and reduce the spatial dimensions of the data. Meanwhile, the decoder component consists of two blocks, each containing one transposed convolutional layer [70] and two normal convolutional layers with a kernel size of three. The use of transposed convolutional layers in the decoder allows the model to up-sample the feature maps and generate a high-resolution output image that closely resembles the ground truth image. The normal convolutional layers that follow the transposed convolutional layers help to refine the features and details in the output image. The decoder ends with a final convolutional layer that produces the final output image. To arrive at this particular architecture in this study, several modifications were tested, such as altering the activation functions, adding or removing convolutional layers, and increasing the number of blocks. The final architecture was chosen based on its ability to produce high-quality output images that accurately represent the ground truth images while minimizing the computational

resources required for training. Figure 4 shows the graphical representation of this architecture along with dimensions of each layer.

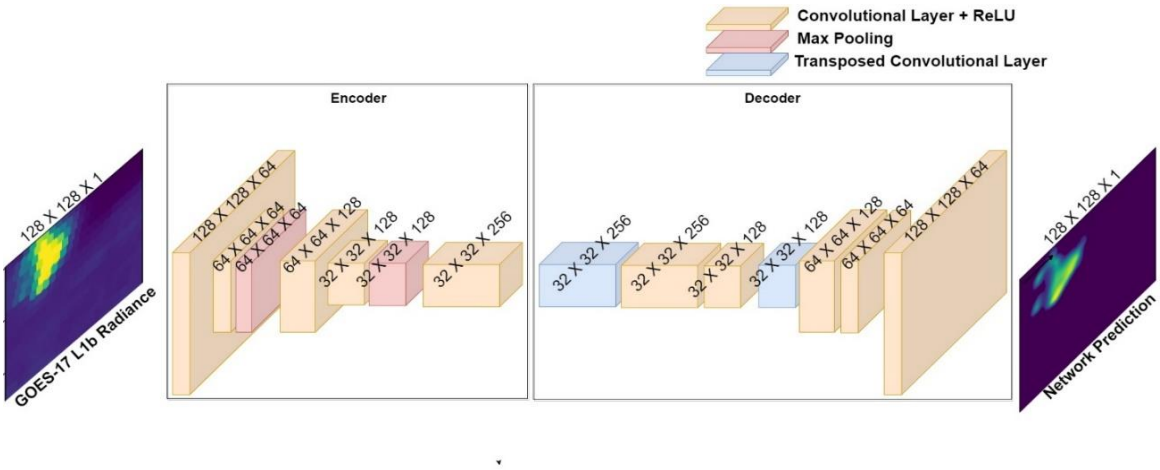

Figure 4: Proposed Autoencoder architecture.

2.2. Loss Functions and Architectural Tweaking

The objective of the study is to enhance GOES-17 imagery by improving its spatial resolution and removing background information, as well as predicting improved radiance values. To achieve this, an ablation study is conducted on four cases, which involve variations in loss functions and autoencoder architecture, in order to determine the optimal solution. The four loss functions, global root mean square error, global plus local root means square error, Jaccard loss, global root mean square error plus Jaccard loss, are explained in detail in following sections.

2.2.1. Global Root Mean Square Error (GRMSE)

Root mean square error (RMSE) is a regression loss function that is commonly used in image reconstruction and denoising tasks [71], where the goal is to minimize the difference between the original and ground truth values. In this study, the autoencoder

model is initially trained using the RMSE loss function on the entire input image, globally, to predict the radiance value for each input image pixel based on the VIIRS ground truth data. This is referred to as the global RMSE (GRMSE) (Eq. 1) to distinguish it from other RMSE-based losses, which will be discussed in the next section.

$$GRMSE = \sqrt{\frac{\sum_{i=1}^{n}(y_i - \hat{y}_i)^2}{n}} \tag{1}$$

where y_i represents the radiance value at the *i*th pixel in the VIIRS ground truth image, $\hat{y}_i$ represents the radiance value at *i*th pixel in the predicted image, and *n* represents the total number of pixels in the VIIRS/predicted image. In the rest of the paper, this setup will be referred to as the GRMSE model.

2.2.2. Global Plus Local RMSE (GLRMSE)

Since the background area is significantly larger than the fire area (e.g., see Fig 1c), it dominates the RMSE calculation. For this reason, a local RMSE (LRMSE) is defined. The LRMSE applies only on the fire area of ground truth, i.e., where pixel's radiance value is non-zero.

$$LRMSE = \sqrt{\frac{\sum_{i=1}^{n}(y_i - \hat{y}_i)^2 \cdot I}{\sum_{i=1}^{n} I}} \qquad I = \begin{cases} 1, y_i \neq 0 \\ 0, otherwise \end{cases} \tag{2}$$

where *I* is the identifier variable, which is one for fire area and zero for background. Based on this, the RMSE is calculated only for fire region of VIIRS ground truth image. The LRMSE is used in addition to global RMSE to result in global plus local RMSE loss function as defined below.

$$GLRMSE = W_G * GRMSE + W_L * LRMSE \quad (3)$$

where W_G is a weight factor for Global RMSE and W_L is a weight factor for Local RMSE. These weights are determined through hyperparameter optimization as will be discussed later. In the rest of the paper, this setup will be referred to as the GLRMSE model.

2.2.3. Jaccard Loss (JL)

For effective wildfire monitoring, it is crucial to not only minimize discrepancies in radiance values but also to predict the wildfire perimeters. This is enabled by binary segmentation. Binary segmentation assigns a binary value to each pixel based on its category, partitioning the image into foreground (i.e., fire region) and background regions [72]. The Jaccard loss function (Eq. 4) is a prevalent loss function utilized in the field of image segmentation [74]. It aims to evaluate and improve the similarity between the predicted and ground truth binary masks (also referred to as segmentation masks).

$$\text{JL} = -\frac{\sum_1^n y_{b,i} \cdot \hat{y}_{b,i}}{\sum_1^n y_{b,i} + \sum_1^n \hat{y}_{b,i} - \sum_1^n y_{b,i} \cdot \hat{y}_{b,i}} \quad (4)$$

where $y_{b,i}$ represents the presence (1) or absence (0) of fire in the VIIRS ground truth image at *i*th pixel, and $\hat{y}_{b,i}$ represents the probability of fire in the predicted image at *i*th pixel.

In order to employ the Jaccard loss function for autoencoder training, the VIIRS ground truth is transformed into a binary mask by setting the radiance value of all fire pixels to one, while keeping the radiance value of background pixels at zero [73]. Additionally, the final activation layer of the autoencoder is modified from ReLu to sigmoid [74],

generating a probability map for every pixel in the output image. The map assigns a score between zero and one to each pixel, indicating the probability of that pixel belonging to the fire region. Once the model is properly trained, the resulting predicted probability map will be converted to binary values. Therefore, we can use this probability map to accurately identify the fire region and distinguish it from the surrounding environment. In the rest of the paper, this setup will be referred to as the JL model.

2.2.4. RMSE Plus Jaccard Loss Using Two-Branch Architecture

RMSE and Jaccard loss are combined to accurately predict the shape, location as well as radiance values of fire. However, as these loss functions require different activation layers, combining them in a single network necessitates architectural changes. To address this issue, a two-branch architecture is employed, where the first branch uses ReLu as the last activation layer to predict images with radiance values, while the second branch uses a sigmoid activation layer to predict the fire probability map. The resulting architecture combines two loss functions (Eq. 5) to enhance the learning and improve predictions. The two-branch architecture, illustrated in Figure 5, branches out before the final convolutional layer. The outputs from the two branches are compared with different ground truth values to calculate individual losses, which are then combined to train the model. This approach enables the weight updating (learning) process to utilize information from both branches, resulting in a more effective training process. As a result, the output from the RMSE branch, which captures both the predicted location and radiance value of the wildfire, is considered the primary output of the model. In this context, RMSE refers to the globally applied GRMSE (Eq. 1). In the rest of the paper, this setup will be referred to as the TBL model.

$$TBL = W_R * GRMSE + W_J * JL \quad (5)$$

where W_R is weight for *GRMSE*, W_J is weight for *JL*, and *TBL* is two-branch loss which is weighted sum of both losses. These weights are determined through hyperparameter optimization.

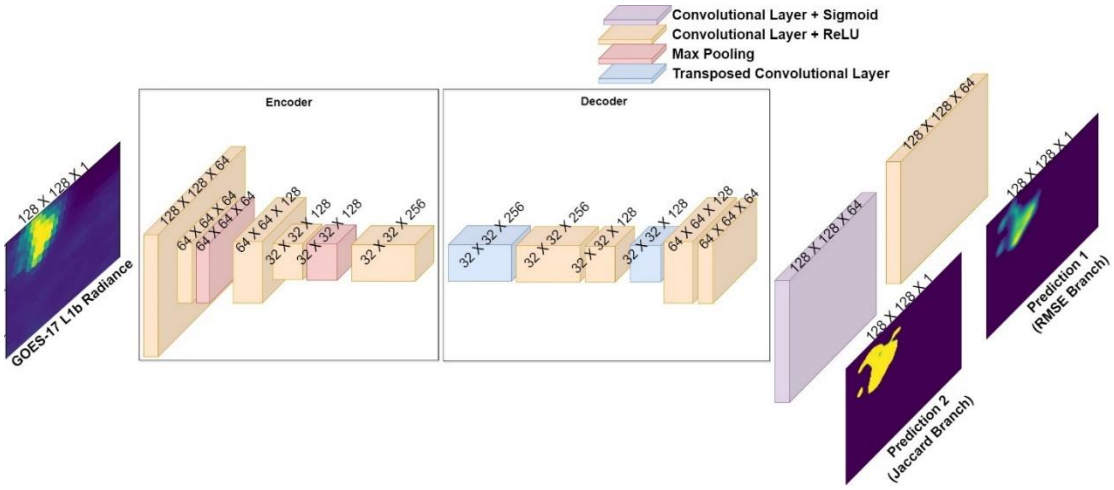

Figure 5: Two-branch autoencoder architecture.

2.3. Evaluation

2.3.1. Pre-Processing for Evaluation: Removing Background Noise

Accurate prediction evaluation requires taking noise into account. Although such noise may not have significant physical relevance, due to their very low radiance compared to actual fire, it can still impact the accuracy of the evaluation metrics. To mitigate this issue, the Otsu thresholding method is used to effectively remove background noise and improve the evaluation process. The method automatically determines the optimal threshold level that separates the foreground (relevant data) from the background (noise) [75]. This is accomplished by calculating the variance between two classes of pixels (foreground and background) at different threshold levels and selecting the threshold

level that maximizes the variance between these two classes. Figure 6 shows the process of using Otsu's thresholding to remove background noise from the prediction (Figure 6a) and create a post-thresholding prediction (Figure 6b) that is compared to the ground truth (Figure 6c) to evaluate the performance of the model. The successful removal of background by Otsu's thresholding improves the alignment between the evaluation metric and visual inspection.

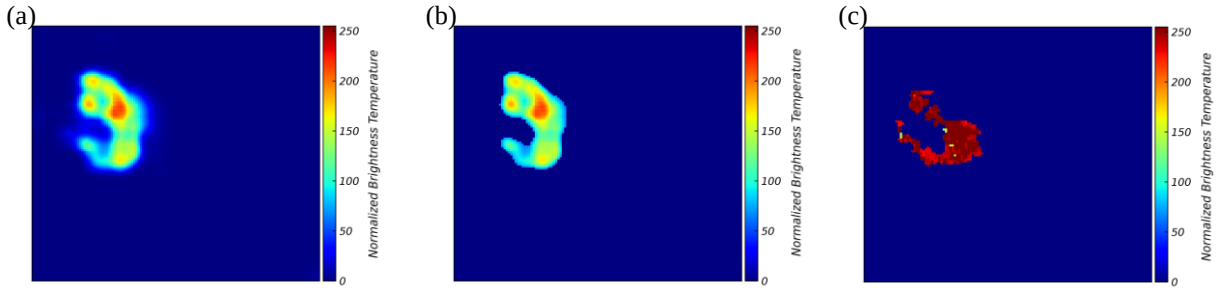

Figure 6: Illustration of Otsu's thresholding on model prediction (a) model prediction, (b) post-thresholding model prediction, (c) ground truth.

2.3.2. Evaluation Metrics

The performance of DL models is evaluated using two metrics: intersection over union (IOU) and intersection's point signal-to-noise ratio (IPSNR), which is a modified version of PSNR used in this study. These metrics will be explained in this section.

IOU (Eq. 6) measures the agreement between the prediction and ground truth by quantifying the degree of overlap of the fire area between them.

$$IOU = \frac{\sum_1^n y_{b,i} \cdot \hat{y}_{b,i}}{\sum_1^n y_{b,i} + \sum_1^n \hat{y}_{b,i} - \sum_1^n y_{b,i} \cdot \hat{y}_{b,i}} \quad (6)$$

The terms used in this equation are already defined following Eq. 4. However, the Eq. 6 and Eq. 4 differ in sign. To compute the IOU metric, both the post-thresholding prediction and ground truth images are converted into binary masks. This is achieved by

setting all non-zero radiance values in the images to one, effectively binarizing the image. This step is necessary to simplify the IOU calculation (Eq. 6). By representing the images as binary masks, the IOU can be calculated as the intersection of the two masks divided by their union, providing an accurate measure of the overlap between the predicted fire region and the ground truth fire region.

On the other hand, IPSNR (Eq. 7) quantifies the similarity in radiance values in the intersection of the fire areas between the prediction and its ground truth images. Here the intersection is defined as the region of images where both prediction and VIIRS ground truth have non-zero radiance (Eq. 8).

$$IPSNR = log_{10}(maxval/IRMSE) \tag{7}$$

$$IRMSE = \sqrt{\frac{\sum_{i=1}^{n}(y_i - \hat{y}_i)^2 \cdot I}{\sum_{i=1}^{n} I}} \qquad I = \begin{cases} 1, y_i.\widehat{y_i} \neq 0 \\ 0, otherwise \end{cases} \tag{8}$$

where *maxval* is maximum radiance value of pixels in the VIIRS image and *IRMSE* is RMSE computed solely for the intersecting fire area using identifier variable *I* which is assigned a value of one for areas where the predicted fire intersects with the VIIRS ground truth, and zero for all other areas.

The motivation for utilizing IPSNR stems from the difficulty of evaluating a model's performance based on the similarity of radiance values, given that the fire area typically occupies only a small portion of the image. If the model's prediction is incorrect, most of the background still appears similar to the ground truth, resulting in higher PSNR values that do not necessarily reflect accurate performance. Therefore, to obtain more reliable evaluation metrics, it is crucial to focus on accurately assessing only the predicted fire

area that matches the ground truth (Eq. 8) when calculating PSNR. It should be noted that the underlying principle of IPSNR is different from that of LRMSE. IPSNR evaluates the quality of the corrected predicted fire area (i.e., pixels predicted as fire, that are also present in ground truth) by considering the RMSE for the intersecting area of prediction and VIIRS ground truth (as described in Eq. 8), while LRMSE is a loss function which focuses on reducing the RMSE specifically for the VIIRS ground truth fire area (as described in Eq. 2).

2.3.3. Dataset Categorization for Evaluation

In addition, to obtain a more accurate and precise evaluation of a model's performance, it's important to account for the diversity of input and ground truth samples. Factors such as fire orientation, location, background noise percent coverage, fire size, and the similarity between input and ground truth can vary significantly and have a considerable impact on the model's performance. Relying solely on evaluating the model's performance on the entire testing set may not provide an accurate assessment, as will be shown later, since the average evaluation may be biased towards the majority of sample types. To overcome this limitation, the dataset is divided into four categories based on two factors: the total coverage of distinguishable foreground in GOES image as well as the initial IOU between the distinguishable foreground in GOES input and VIIRS ground truth.

To achieve this, Otsu thresholding is used again to eliminate background information from the original GOES image (Figure 7a), resulting in a post-thresholding GOES image (Figure 7b) with distinguishable foreground information that is used to compute coverage

and initial IOU. Coverage is determined by calculating the ratio of non-zero radiance pixels to the total number of pixels in the post-thresholding image. This metric indicates the degree of foreground presence in the GOES image. Meanwhile, the initial IOU is calculated between the binarized post-thresholding GOES input and binarized VIIRS ground truth. This provides an indication of the degree of foreground area similarity between the two images. It is important to note that the foreground identified by Otsu in the GOES input image may not always accurately indicate the fire region, unlike the prediction image. In some cases, the radiance value of the background may be comparable to, or even greater than, that of the actual fire region, making it difficult to identify the fire accurately. Additionally, the coverage calculation involves a single iteration of Otsu thresholding, which is used to determine the true coverage of GOES. On the other hand, calculating IOU requires multiple iterations of Otsu thresholding to accurately assess only the fire area. The final IOU result is obtained by selecting the highest IOU value obtained from all iterations, ensuring that only the fire area is considered for evaluation.

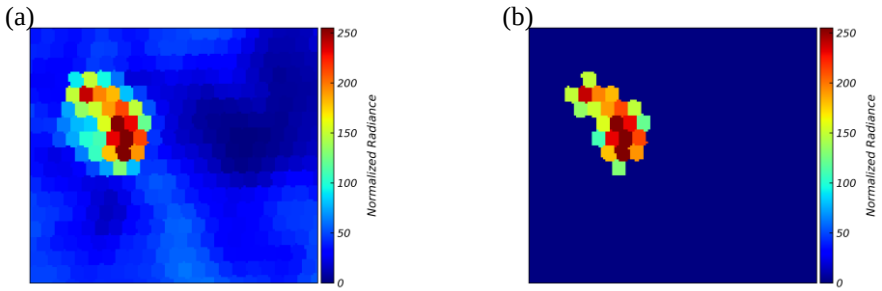

Figure 7: Otsu's thresholding on original GOES (a) input GOES image, (b) post-thresholding GOES image.

The dataset for evaluation is categorized into four groups based on the calculated coverage and IOU. These groups are low coverage with high IOU (LCHI), low coverage with low IOU (LCLI), high coverage with high IOU (HCHI), and high coverage with low

IOU (HCLI). Threshold values for coverage and IOU are determined through visual inspection of the results and are provided in Table 1. By categorizing the dataset, we can perform a more accurate evaluation of the model's performance and identify its strengths and weaknesses in various scenarios.

Table 1: Condition for each dataset category

Category	**LCHI**	**LCLI**	**HCHI**	**HCLI**
Condition	Coverage < 20% IOU > 5%	Coverage < 20% IOU < 5%	Coverage > 20% IOU > 5%	Coverage > 20% IOU < 5%

3. Result

3.1. Training

In this study, the western U.S. wildfire events that occurred between 2019 and 2021 (listed in Appendix A) are utilized to create contemporaneous images of VIIRS and GOES using the preprocessing steps explained in Section 2. The preprocessed images are then partitioned into windows of size 128 by 128 pixels, resulting in a dataset of 5,869 samples, which are used as input and ground truth for the DL model. These samples are split with ratio of 4 to 1 to obtain training and testing dataset (i.e., 80% for training and 20% for testing). The training set is further split with 4 to 1 ratio to get training and validation set. After splitting the dataset, the training, validation, and testing set include 3756, 939, and 1174 samples, respectively. The validation set is used to monitor for overfitting during the training process, while the testing set is kept aside for evaluating the final performance of the model. Additionally, to improve the diversity of the training data and prevent overfitting, data augmentation techniques are utilized. In particular, at each epoch, the training samples undergo random horizontal and vertical flips, leading to

greater variability in the training data and improving the model's generalization to new and unseen data.

Hyperparameter tuning is done using weights and biases (WAB) tool [76], to estimate the optimal hyperparameters through random sampling from the hyperparameter space. After training is completed on each subset of hyperparameters, the validation loss results, and overfitting analysis are evaluated to determine the best performing hyperparameters. he hyperparameter subset that leads to the smallest validation loss and overfitting are then chosen as the final hyperparameters. When autoencoder models combine two losses, such as GLRMSE and the TBL model, the weights of each loss function are also considered as hyperparameters and are determined through the same hyperparameter tuning process.

Based on the hyperparameter tuning, all four cases of autoencoder model, outlined in Section 3.2, are trained for 150 epochs and batch size of 16 using Adam optimizer with learning rate of 3×10^{-5} [77]. A learning rate decay based on validation loss plateau, with weight decay of 0.1, threshold of 1×10^{-5}, and patience of 10 epoch, is used during training to help in both optimization and generalization[78]. Moreover, for the GLRMSE case, the best results are achieved when the weights of the local RMSE and global RMSE are set to 1 and 9. Meanwhile, for the TBL model, the best results are obtained when the weights of RMSE and Jaccard loss are set to 3 and 1 for combining the two losses. The DL model is developed using Pytorch [79] (v. 1.12) Python package and trained on an Nvidia RTX 3090 Graphical Processing Unit (GPU) with 24 GB of Video RAM (VRAM). Figure 8 depicts the training curve for all four cases along with individual

losses function of GLRMSE and TBL model. As can be seen, the loss functions are converging to a plateau with small to no overfitting.

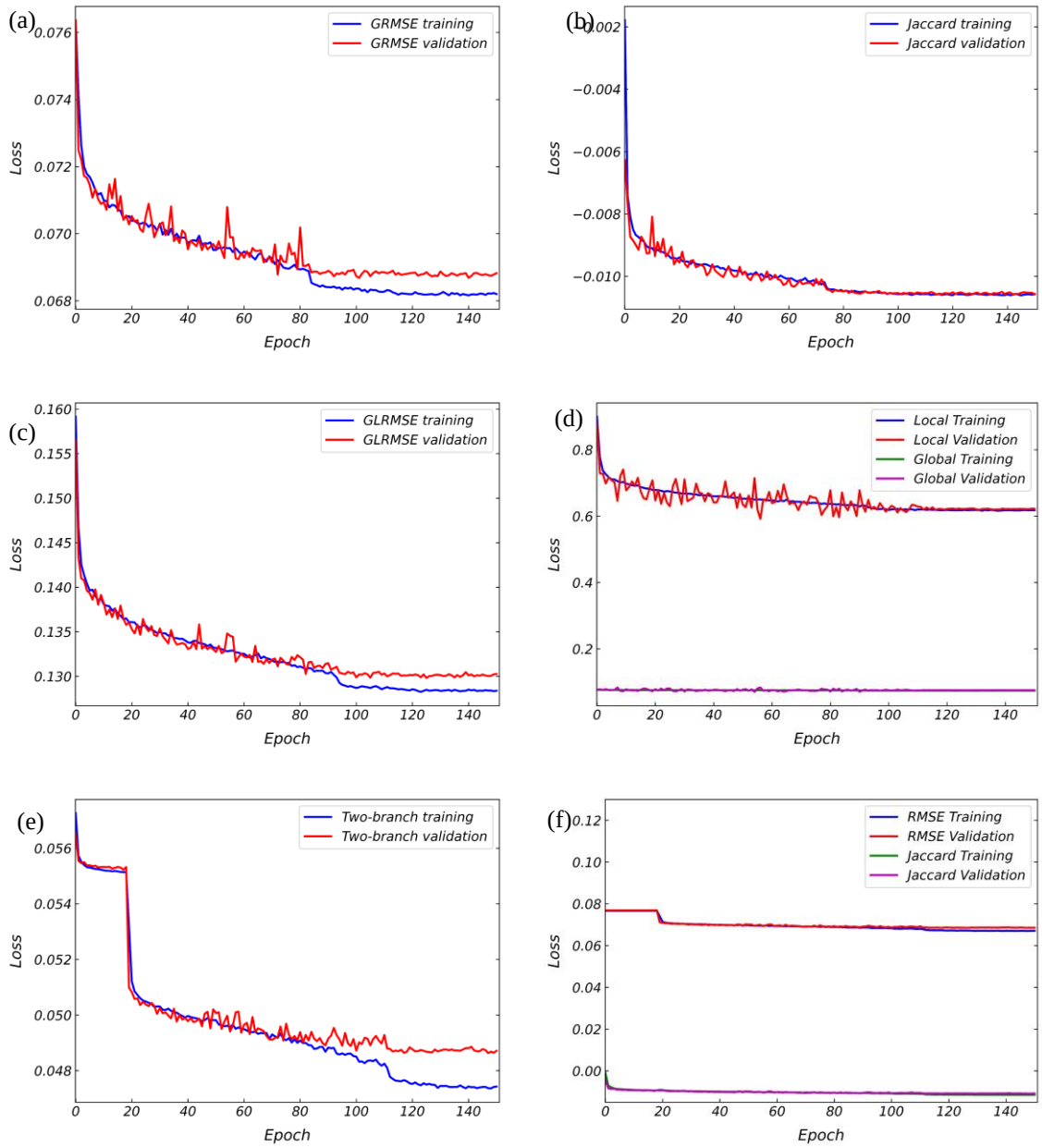

Figure 8: Training curves (i.e., Loss vs Epoch) of (a) GRMSE, (b) JL, (c) GLRMSE, (d) individual global and local for GLRMSE loss, (e) TBL, (f) individual RMSE and Jaccard loss for TBL.

3.2. Testing

To evaluate the performance of the four samples, IOU and IPSNR are used as the evaluation metrics, and the results are presented in Table 2 for the entire testing set. The TBL model is found to produce the best results in terms of IOU of prediction and ground truth (VIIRS) while GLRMSE produces the best results in terms of IPSNR. This suggests that the TBL model is influenced by both its loss function (i.e., Jaccard loss for the fire shape and GRMSE for radiance values) resulting in a higher IOU. On the other hand, GLRMSE improves the radiance values prediction in the fire area by adding local (i.e., fire area of ground truth) RMSE calculation resulting in a higher IPSNR. However, as discussed earlier in Section 3.3, there is a possibility of evaluation bias towards the majority of the sample types. Therefore, the evaluation is further carried out on the four categories, namely LCHI, LCLI, HCHI, and HCLI. Within each group, an analysis is conducted on three distinct samples to examine the sample's performance visually, and the average evaluation score for each category is also provided. This process can lead to a more comprehensive understanding of the strengths and weaknesses of each model.

Table 2: Evaluation of total testing sample for four models

Evaluation Matrix	**GRMSE**	**GLRMSE**	**JL**	**TBL**
IOU	0.1285	0.1242	0.1244	0.1320
IPSNR	40.5120	42.8047	N/A	40.8669

3.2.1. LCHI: Low Coverage with High IOU

Figure 9 depicts the image captured by GOES and VIIRS along with the results of the four models for Windy Fire on 2021-09-18 at 21:36 UTC. Due to the small size of the distinguishable pixels found after applying Otsu thresholding, this sample is classified as

having low coverage. Furthermore, the initial IOU between the fire areas in the GOES and VIIRS images is relatively high indicating a significant overlap in the fire area captured by both satellites. This type of scenario is generally less challenging for the DL models to handle, as there is a clear and visible overlap between the fire areas in both images.

As can be seen, the main observation of this sample is that the JL model performs better than the GRMSE and GLRMSE models in accurately predicting the location of fires, with an IOU score of 0.420, compared to 0.390 and 3.760, respectively. The visual results demonstrate that the JL can predict concavity in the shape of fires, a feature that the GRMSE and GLRMSE models cannot capture likely due to their loss function that focuses more on the radiance values. However, in terms of predicting radiance values, the GLRMSE model outperforms other models, with an IPSNR of 57.54, followed by the GRMSE model at 55.11 and the TBL model at 54.05. The visual results confirm that the radiance values predicted by the GLRMSE model are higher than other models and hence closer to the ground truth. Furthermore, the TBL improves the prediction accuracy compared to the JL, achieving an IOU score of 0.435. Although this improvement comes at the cost of a lower IPSNR score, the TBL model provides a compromise between predicting radiance values and accurately capturing the shape of wildfires.

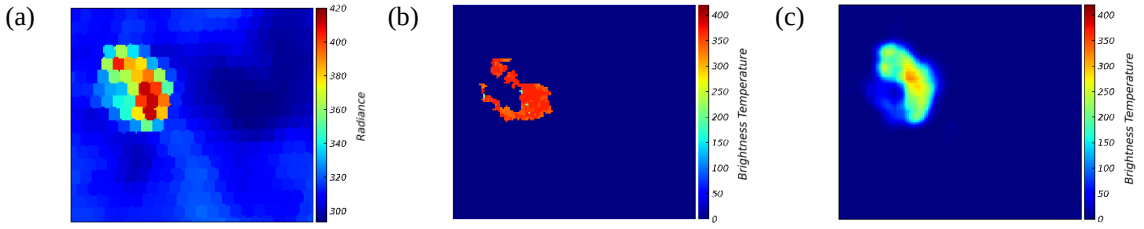

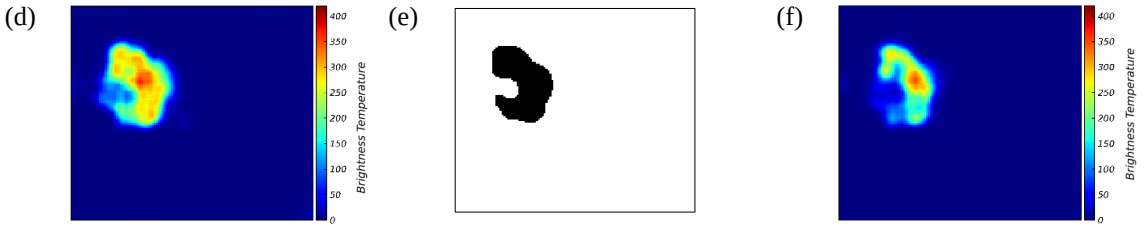

Figure 9: Windy Fire on 2021-09-18 21:36 UTC (a) GOES input, (b) VIIRS ground truth, and results from (c) GRMSE, (d) GLRMSE, (e) JL, and (f) TBL models, where radiance's units are $\frac{mW}{m^2 sr(cm^{-1})}$ *and brightness temperature's units are K.*

Figure 10 depicts the image captured by GOES and VIIRS along with results from the four models for Monument Fire on 2021-08-29 at 21:12 UTC. In contrast to the previous sample, the JL model has lower IOU score of 0.162 while the GRMSE and GLRMSE models achieved higher IOU scores of 0.199 and 0.200, respectively. This can be due to the GOES fire in this sample having a relatively low radiance value or VIIRS fire spanning across multiple clusters, unlike the previous sample. In this sample, the TBL model's IOU score is 0.179, which is lower than that of the GRMSE model. Notably, the TBL model's performance in this sample is consistent with the performance of the JL model, highlighting that the low radiance fire of GOES or multiple cluster shape of the VIIRS fire can negatively affect the performance of the Jaccard model. However, it is worth noting that the GLRMSE model achieved an IPSNR of 52.41, which is still higher than the IPSNRs of both the GRMSE (50.37) and TBL (50.39) models. Figure 9 supports this observation, showing that the GLRMSE model produced higher radiance values than the other models.

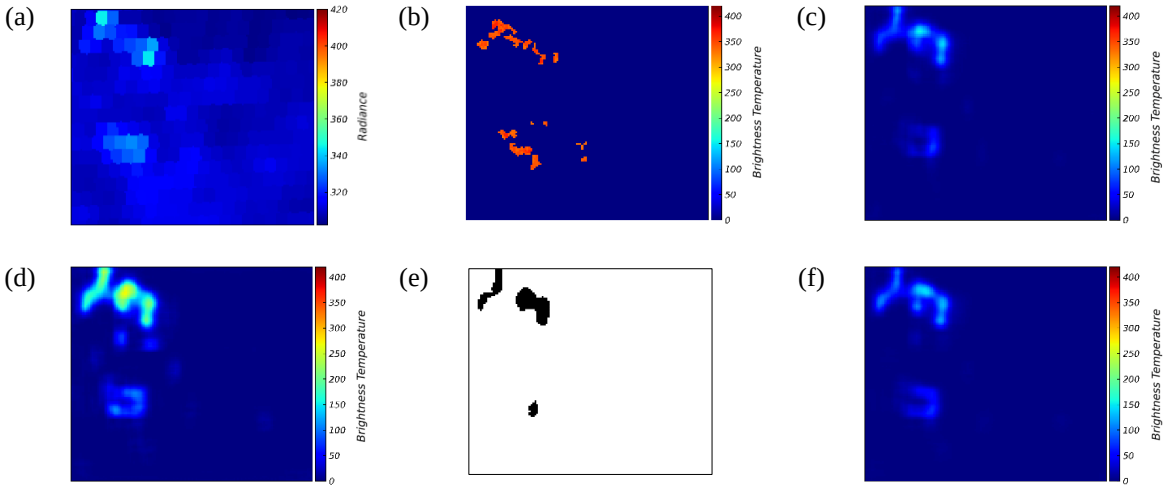

Figure 10: Monument Fire on 2021-08-29 21:12 UTC (a) GOES input, (b) VIIRS ground truth, and results from (c) GRMSE, (d) GLRMSE, (e) JL, and (f) TBL, where radiance's units are $\frac{mW}{m^2 sr(cm^{-1})}$ *and brightness temperature's units are K.*

Figure 11 depicts the image captured by GOES and VIIRS along with results from the four models for French Fire on 2021-09-17 at 8:54 UTC. This sample is very similar to the sample in Figure 9, with GOES and VIIRS fire area concentrated in one region with good initial overlap. The TBL model exhibits superior performance in terms of IOU, followed by the JL, then GRMSE, and finally GLRMSE model. Meanwhile, the GLRMSE model outperforms other models in terms of IPSNR, followed by the GRMSE model and then the TBL model. These results closely follow the pattern observed for the sample in Figure 9.

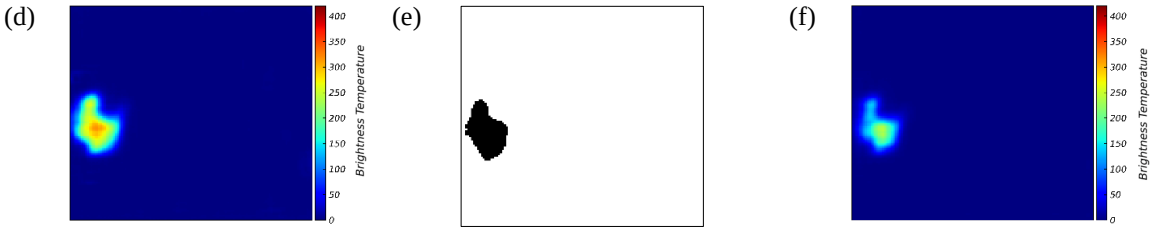

Figure 11: French Fire on 2021-09-17 8:54 UTC (a) GOES input, (b) VIIRS ground truth, and results from (c) GRMSE, (d) GLRMSE, (e) JL, and (f) TBL, where radiance's units are $\frac{mW}{m^2 sr(cm^{-1})}$ *and brightness temperature's units are K.*

Table 3 presents the evaluation results for 281 LCHI testing samples, and the findings reveal a similar pattern to what is observed in the complete dataset. While there may be some exceptions, such as the sample shown in Figure 10, the pattern observed in Figures 9 and 11 appears to be generally consistent with the bulk statistics of this category.

Table 3: Evaluation of LCHI testing sample for four losses

Evaluation Matrix	**GRMSE**	**GLRMSE**	**JL**	**TBL**
IOU	0.2766	0.2637	0.2694	0.2825
IPSNR	52.2926	55.3788	N/A	52.7992

Therefore, it can be concluded that, for most of the samples in this category, the model's performance follows a similar pattern. Specifically, the TBL model performs the best among the models in terms of IOU, indicating better agreement between the predicted and actual fire areas. This can be attributed to the fact that this model is trained based on both fire shape and radiances based on its loss function. Meanwhile, the GLRMSE model has the highest IPSNR, indicating better performance in predicting radiance values. This suggests that the GLRMSE model can predict radiance values closer to the VIIRS, likely due to the focus of the local term of its loss function on the fire area.

3.2.2. LCLI: Low Coverage with Low IOU

Figure 12 depicts the image captured by GOES and VIIRS along with results from the four models for Jack Fire on 2021-07-21 at 20:00 UTC. In this sample, all models produce an IOU score of zero due to the small size of the VIIRS fire and the lack of significant overlap between the GOES and VIIRS images. This is expected as there is no underlying pattern in these types of samples that the DL model can learn from.

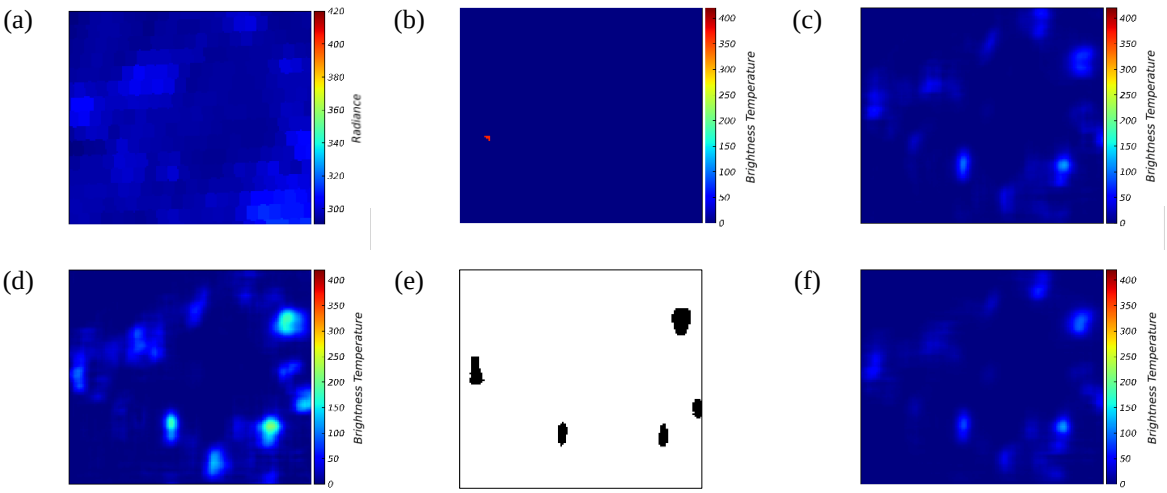

Figure 12: Jack Fire on 2021-07-21 20:00 UTC (a) GOES input, (b) VIIRS ground truth, and results from (c) GRMSE, (d) GLRMSE, (e) JL, and (f) TBL, where radiance's units are $\frac{mW}{m^2 sr(cm^{-1})}$ *and brightness temperature's units are K.*

Figure 13 depicts the image captured by GOES and VIIRS along with results from the four models for Antelope Fire on 2021-08-21 at 20:18 UTC. In this sample, the VIIRS fire area is relatively small but larger compared to the previous sample. Although there are small clusters of fire, they are in close proximity to each other compared to the LCHI sample from Figure 10. Making this case even more challenging, the GOES image does not show any visible fire area. Despite these difficult conditions, all four models show reasonable performance in predicting the fire location. Among these models, the JL model demonstrates a significant improvement over the GRMSE model, with an IOU

score of 0.148 compared to 0.07. The TBL shows little improvement with an IOU score of 0.08. Even though the TBL model is not the best in terms of IOU, it still show improvement over GRMSE. The GLRMSE model shows the best radiance value prediction in terms of IPSNR.

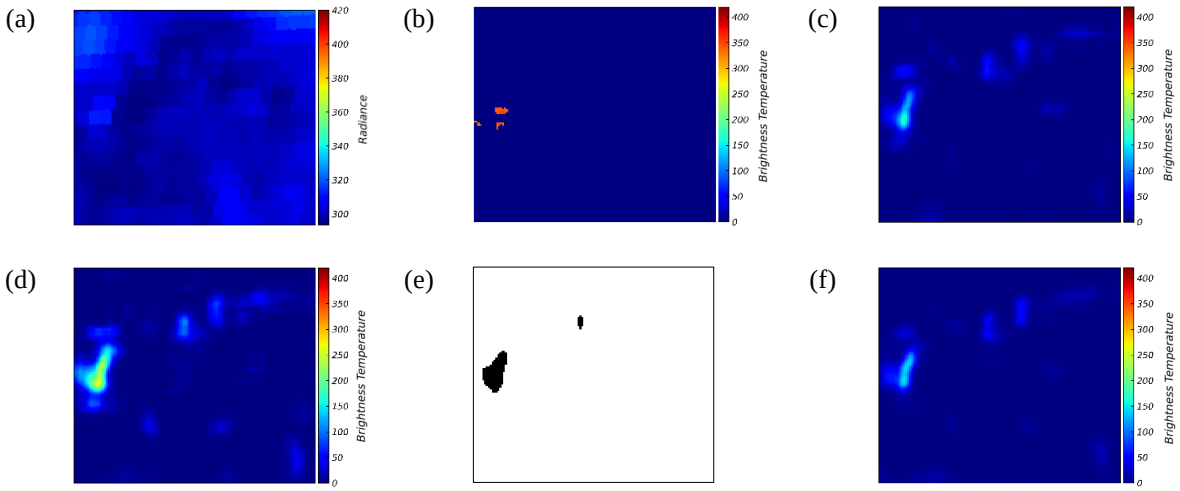

Figure 13: Antelope Fire on 2021-08-21 20:18 UTC (a) GOES input, (b) VIIRS ground truth, and results from (c) GRMSE, (d) GLRMSE, (e) JL, and (f) TBL, where radiance's units are $\frac{mW}{m^2 sr(cm^{-1})}$ *and brightness temperature's units are K.*

Figure 14 depicts the image captured by GOES and VIIRS along with results from the four models for Monument Fire on 2021-08-08 at 21:00 UTC. In this sample, the distinguishable area in the GOES image has low coverage and is dissimilar in shape and orientation to the VIIRS fire. Additionally, the VIIRS fire area is scattered into multiple clusters, similar to the LCHI sample from Figure 10. As a result, accurately predicting the fire location posed a challenge for all four models. The JL model produced an IOU score of only 0.040, lower than the GRMSE model's score of 0.090, a pattern similar to the one observed in the sample of Figure 10. These results suggest that the JL model may not be effective in samples where the VIIRS fire area is scattered and dispersed. Nonetheless, like previous results GLRMSE has the best radiance value prediction.

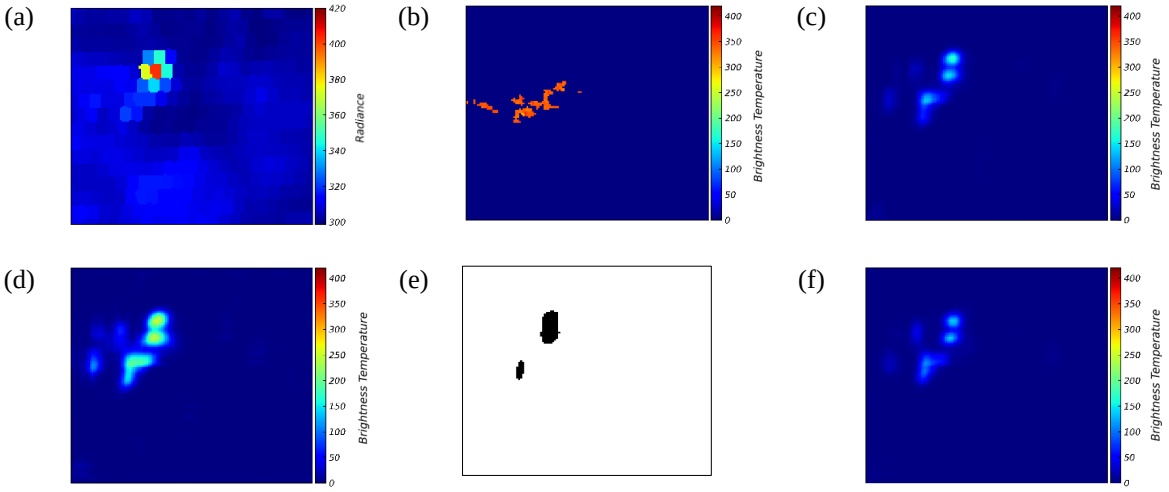

Figure 14: Monument Fire on 2021-08-08 21:00 UTC (a) GOES input, (b) VIIRS ground truth, and results from (c) GRMSE, (d) GLRMSE, (e) JL, and (f) TBL, where radiance's units are $\frac{mW}{m^2 sr(cm^{-1})}$ *and brightness temperature's units are K.*

Table 4 presents the evaluation results for 47 LCLI testing samples, revealing a pattern similar to what is observed in the complete dataset. Specifically, the TBL model exhibits better IOU and GLRMSE demonstrates superior IPSNR performance compared to other models. However, for some samples where there is no overlap between GOES and VIIRS fire areas or where VIIRS fire areas are scattered in clusters, the TBL model is not the best performing model. In some cases, the GLRMSE model demonstrates better IOU results than other models. This finding is also supported by Table 4, where the IOU from GLRMSE is better than the GRMSE and JL models and close to TBL model.

Table 4: Evaluation of LCLI testing sample for four losses

Evaluation Matrix	**GRMSE**	**GLRMSE**	**JL**	**TBL**
IOU	0.0376	0.0401	0.0346	0.0416
IPSNR	36.2735	37.7168	N/A	35.2053

3.2.3. HCHI: High Coverage with High IOU

Figure 15 depicts the image captured by GOES and VIIRS along with results from the four models for Windy Fire on 2021-09-14 at 21:06 UTC. In this sample, the GOES image is considered to have high coverage due to the large area of background information with high radiance values that are not removed by Otsu thresholding. However, the actual fire in GOES still has good overlap with VIIRS. The predictions of all models remove most of the background information and predict the fire area similar to the ground truth. Although the JL model results in a lower IOU score of 0.287 compared to the GRMSE model's score of 0.310, the TBL model achieves an IOU score of 0.317, suggesting that the JL model does not need to perform better than GRMSE for TBL to perform best, as observed in previous samples. Similar to previous samples, GLRMSE performs best in terms of IPSNR.

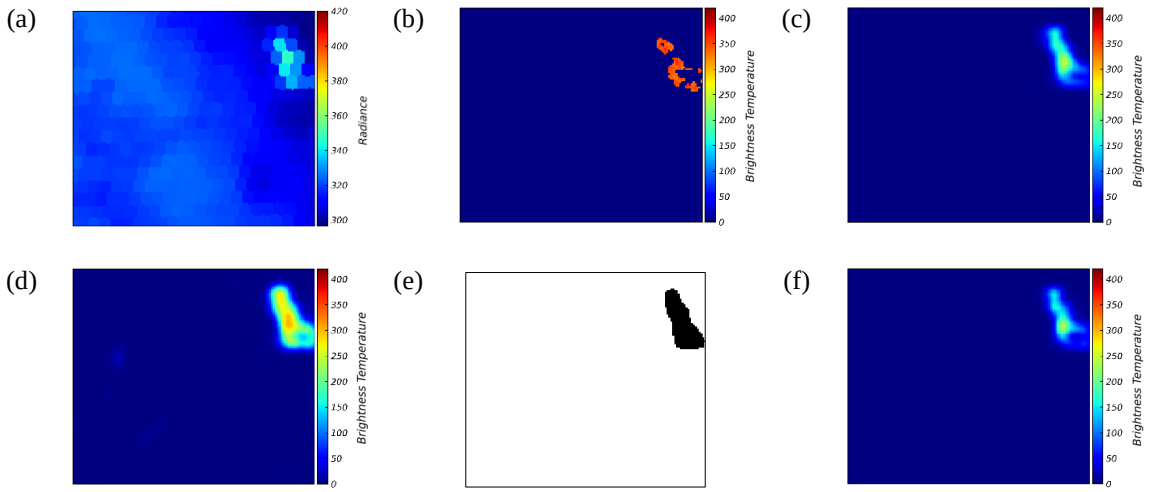

Figure 15: Windy Fire on 2021-09-14 21:06 UTC (a) GOES input, (b) VIIRS ground truth, and results from (c) GRMSE, (d) GLRMSE, (e) JL, and (f) TBL, where radiance's units are $\frac{mW}{m^2 sr(cm^{-1})}$ *and brightness temperature's units are K.*

Figure 16 depicts the image captured by GOES and VIIRS along with results from the four models for CZU (Cal Fire designation for its San Mateo–Santa Cruz Unit) Lighting

Complex Fire on 2020-08-20 at 21:18 UTC. In this sample, the JL model had a lower IOU score of 0.181 compared to the GRMSE model's score of 0.313. This difference in performance may be because the VIIRS fire area is a scatter region as discussed previously. The TBL model, however, achieved the highest IOU score of 0.354. Although the visual results for the GRMSE and TBL models appear similar, the evaluation results suggest that the TBL model is better able to reduce background noise, resulting in a higher IOU score. However, evident from visual inspection as well as IPSNR evaluation, the GLRMSE proved to be predicting better radiance values.

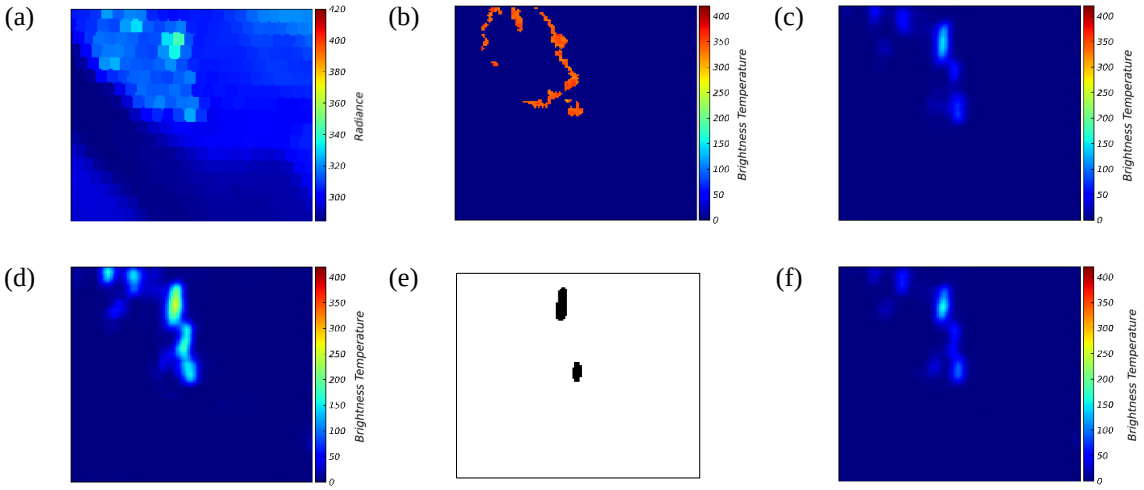

Figure 16: CZU lighting complex Fire on 2020-08-20 21:18 UTC (a) GOES input, (b) VIIRS ground truth, and results from (c) GRMSE, (d) GLRMSE, (e) JL, and (f) TBL, where radiance's units are $\frac{mW}{m^2 sr(cm^{-1})}$ *and brightness temperature's units are K.*

Figure 17 depicts the image captured by GOES and VIIRS along with results from the four models for French Fire on 2021-08-22 at 20:00 UTC. In this sample, the JL model achieved the highest performance with an IOU score of 0.238, while the GRMSE and TBL models had an IOU score of 0.200. The GLRMSE model also performed close to the JL model with an IOU score of 0.232. The GLRMSE model still demonstrates the highest IPSNR score.

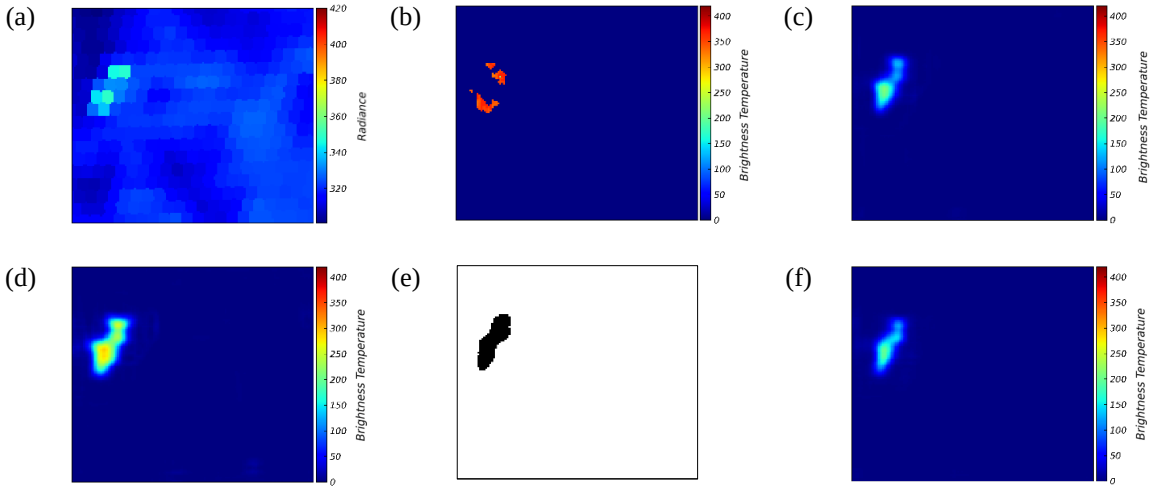

Figure 17: French Fire on 2021-08-22 20:00 UTC (a) GOES input, (b) VIIRS ground truth, and results from (c) GRMSE, (d) GLRMSE, (e) JL, and (f) TBL, where radiance's units are $\frac{mW}{m^2 sr(cm^{-1})}$ *and brightness temperature's units are K.*

Table 5 presents the evaluation results for 267 HCHI testing samples. Although the results demonstrate a consistent pattern of GLRMSE's superior performance in terms of IPSNR compared to other models, but the TBL model falls slightly short compared to the JL model in terms of IOU. Although some samples are found where JL models IOU is significantly lower than other models contradicting the average evaluation (Table 5) for this category, which suggests a need for more precise categorization.

Table 5: Evaluation of HCHI testing sample for four losses

Evaluation Matrix	**GRMSE**	**GLRMSE**	**JL**	**TBL**
IOU	0.1754	0.1656	0.1814	0.1802
IPSNR	51.1771	54.0146	N/A	51.5460

3.2.4. HCLI: High Coverage with Low IOU

Figure 18 depicts the image captured by GOES and VIIRS along with results from the four models for Antelope Fire on 2021-08-17 at 21:36 UTC. In this sample, while the initial overlap between GOES and VIIRS is visually hard to detect, the four models accurately predicted the general location of the fire based on the ground truth. The JL model branch exhibited the best performance with an IOU score of 0.14, compared to GRMSE's score of 0.11, GLRMSE's score of 0.09, and TBL's score of 0.11. The GLRMSE model still demonstrates the highest IPSNR score.

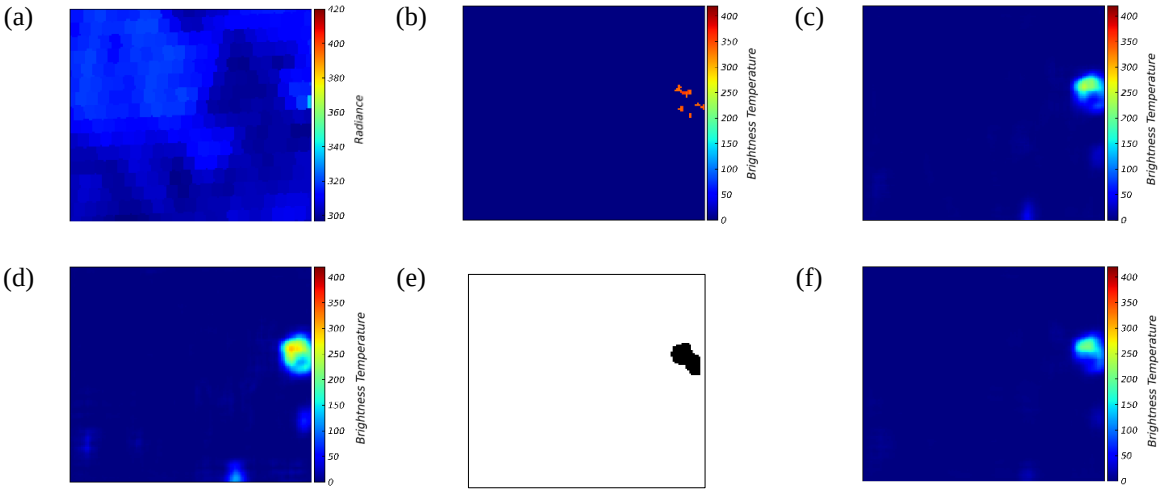

Figure 18: Antelope Fire on 2021-08-17 21:36 UTC (a) GOES input, (b) VIIRS ground truth, and results from (c) GRMSE, (d) GLRMSE, (e) JL, and (f) TBL, where radiance's units are $\frac{mW}{m^2 sr(cm^{-1})}$ *and brightness temperature's units are K.*

Figure 19 depicts the image captured by GOES and VIIRS along with results from the four models for Magnum Fire on 2020-06-16 at 20:00 UTC. In this sample, the JL model had the lowest predicted IOU score of 0.060, compared to 0.170 for both the GRMSE and GLRMSE models, and 0.160 for the TBL model. The inferior performance of the JL model may be attributed to the dispersed and scattered fire area in VIIRS. Despite this, the GLRMSE model still demonstrated the highest IPSNR score.

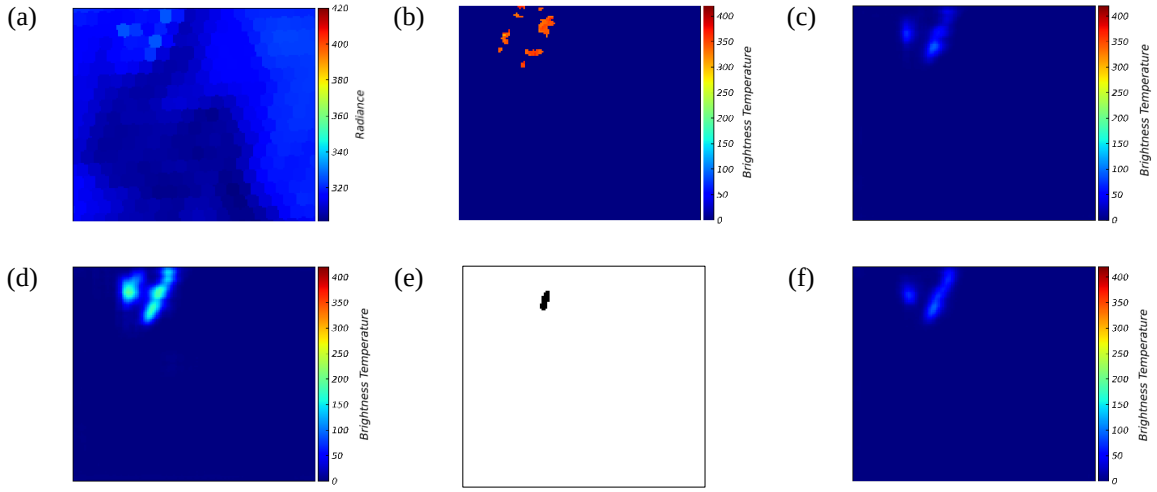

Figure 19: Magnum Fire on 2020-06-16 20:00 UTC (a) GOES input, (b) VIIRS ground truth, and results from (c) GRMSE, (d) GLRMSE, (e) JL, and (f) TBL, where radiance's units are $\frac{mW}{m^2 sr(cm^{-1})}$ *and brightness temperature's units are K.*

Figure 20 depicts the image captured by GOES and VIIRS along with results from the four models for Beachie Fire on 2020-09-13 at 20:30 UTC. In this sample, the high coverage and absence of overlap among the fires result in all models predicting a zero IOU score, indicating incorrect predictions compared to the ground truth. This outcome was expected due to the small size of the fires in the VIIRS data. However, it is worth noting that all the models successfully removed most of the background information, except for the areas where GOES recorded high radiance values.

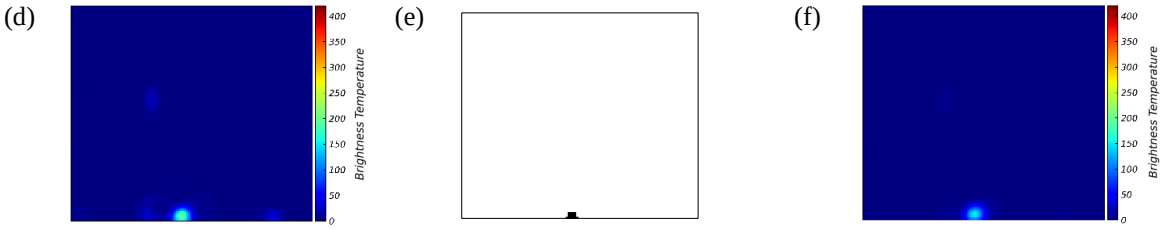

Figure 20: Beachie Fire on 2020-09-13 20:30 UTC (a) GOES input, (b) VIIRS ground truth, and results from (c) GRMSE, (d) GLRMSE, (e) JL, and (f) TBL, where radiance's units are $\frac{mW}{m^2 sr(cm^{-1})}$ *and brightness temperature's units are K.*

Table 6 presents the evaluation results for 579 HCLI testing samples. Although the results demonstrate a consistent pattern of GLRMSE's superior performance in terms of IPSNR compared to other models, the TBL model falls slightly short compared to the GLRMSE loss model in terms of IOU evaluation.

Table 6: Evaluation of HCLI testing sample for four losses

Evaluation Matrix	**GRMSE**	**GLRMSE**	**JL**	**TBL**
IOU	0.0424	0.0442	0.035	0.0441
IPSNR	30.2206	31.9460	N/A	30.6110

3.3. Blind Testing

To evaluate the performance of the trained model in real-world situations, the best performing model (i.e., the TBL model based on earlier results as seen in section 4.1) is used for blind testing on two wildfire events, namely the 2020 Bear fire and the 2021 Caldor fire. The term "blind testing" refers to the fact that the DL model has never been exposed to data from these sites during training. To conduct the blind testing, GOES images are downloaded at its operational temporal frequency (i.e., 5 min) for the entire duration of the testing. The preprocessing pipeline as outlined in Section 2.2.1 is then applied to these images, and then fed to the trained DL as input. The output of the DL,

which are enhanced GOES images, are then postprocessed (combining back windows of image, which were created to be used as input for DL model) for visualization. These predicted images are validated against high resolution (i.e., 250 m spatial and 5 min temporal resolution) fire perimeters estimated from NEXRAD reflectivity measurements [80].

Figure 21 shows four instances during the 2020 Bear Fire from September 8 to 9, 2020, with the blue boundaries representing the radar-estimated fire perimeter and color shading representing the output of the DL model. As of 2020-09-08 19:35 UTC, the model's results have good agreement with radar data, but are not completely matching. However, by 2020-09-08 22:25 UTC, the DL model's predictions are comparatively within the radar parameters. As the fire area expands, by 2020-09-09 02:30 UTC, it is still confined by radar parameters, with some area outside. Even as the fire begins to fade and only remains at the boundaries, by 2020-09-09 03:55 UTC, it is still comparatively inside the radar parameters. It should be noted that fitting a fire perimeter to the DL output is out of the scope of this study and will be addressed in future research.

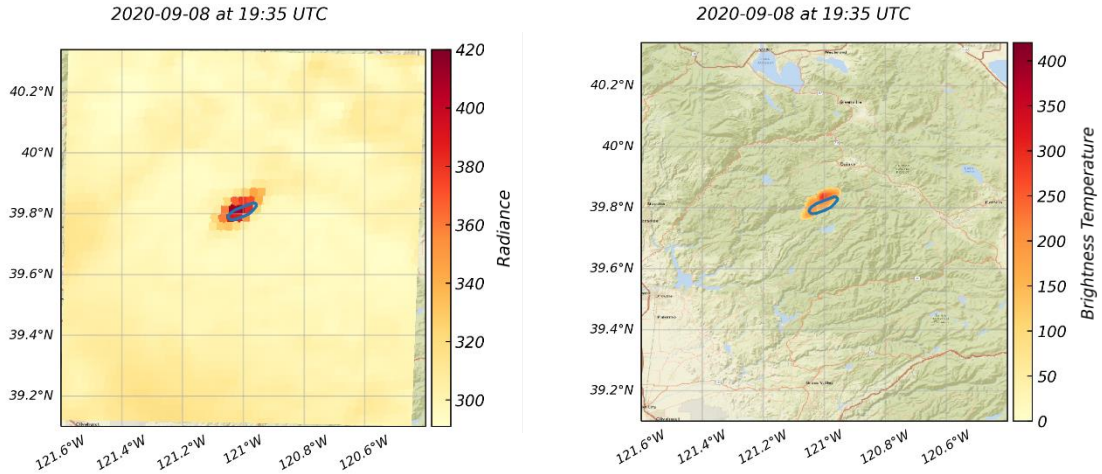

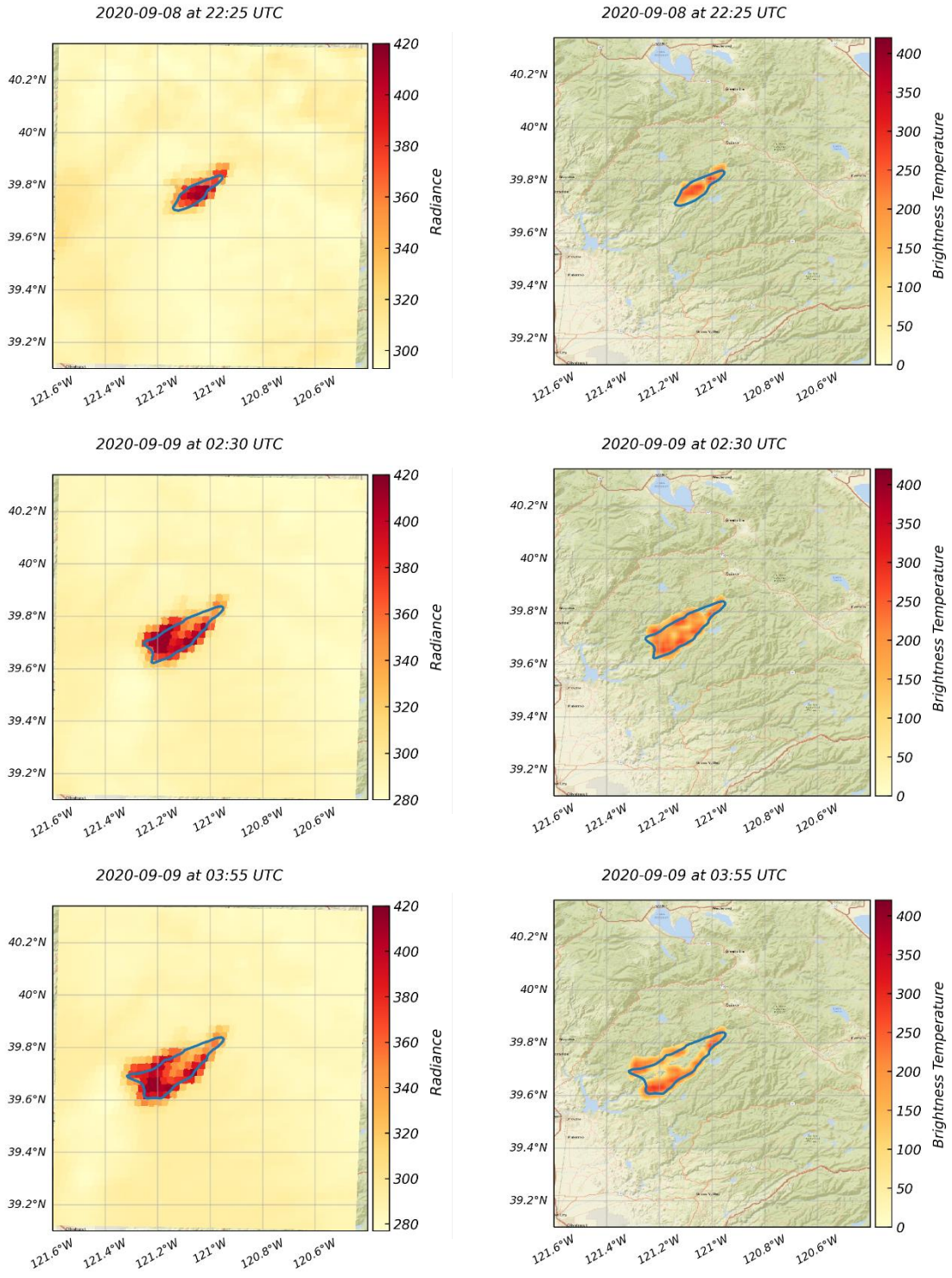

Figure 21: Validation Model prediction with Radar data for Bear Fire at 4 instances, where radiance's units are $\frac{mW}{m^2 sr(cm^{-1})}$ *and brightness temperature's units are K. (left column) shows GOES imagery and (right column) network prediction. Blue boundary depicts radar estimated fire perimeter.*

Similarly, Figure 22 depicts four instances during the 2021 Caldor Fire from August 16 to 17, 2021. Reasonable agreement between the fire pixel and predicted boundaries can be observed in results however not as accurate as in case of Bear fire. At 2021-08-17 17:05 UTC, the network's prediction is aligned with general location of the radar parameters, with no visible fire in the bottom half and overprediction in the top half. From 2021-08-17 20:30 UTC to 2021-08-17 23:55 UTC, the network's prediction is consistently confined by the radar parameters, with some fire area outside, but the overall shape is similar to the radar parameter.

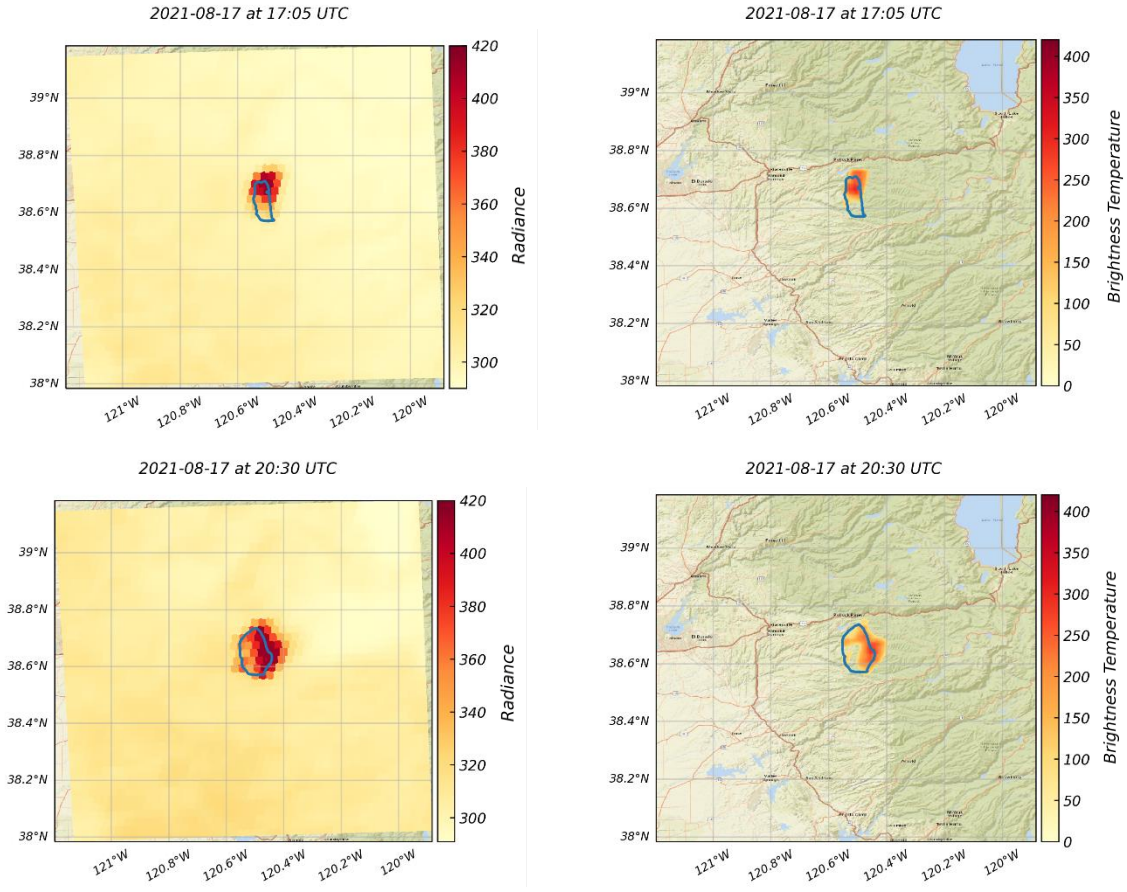

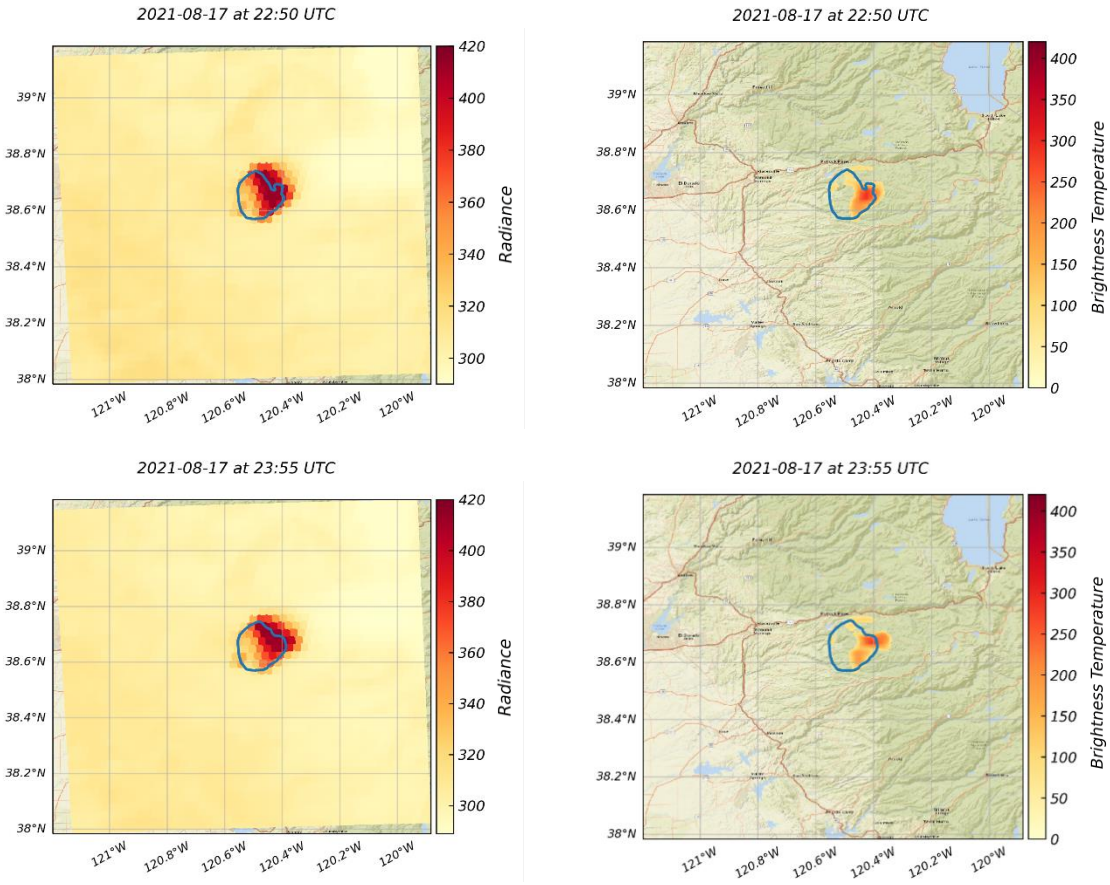

Figure 22: Validation Model prediction with Radar data for Caldor Fire at 4 instances, where radiance's units are $\frac{mW}{m^2 sr(cm^{-1})}$ *and brightness temperature's units are K. (left column) shows GOES imagery and (right column) network prediction. Blue boundary depicts radar estimated fire perimeter.*

The findings suggest that the DL model's predictions closely align with the radar data, indicating that it has the potential to be a valuable tool for predicting wildfires in real-time. It is worth mentioning that both GRMSE and GLRMSE models yielded similar visual results.

Chapter 3: Conclusions

The primary objective of this study was to develop a DL model to improve the spatial resolution of GOES images as well as predicting radiance values, similar to VIIRS ground truth. To achieve this objective, an autoencoder was trained using GOES data as input and VIIRS data as ground truth. An ablation study was conducted to assess the performance of four models, created based on different loss functions and architectural variations in the autoencoder, namely global root mean square error, global plus local root mean square error, Jaccard loss, two-branch loss. The study provided details on the training process and hyperparameters used, along with a comprehensive explanation of the performance and the results obtained from each model. The architecture of the autoencoder, along with the different loss functions used, was discussed in detail, including the mathematical formulas for each loss function. Furthermore, the study addressed the difficulties of assessing model performance and proposed an evaluation metric that aligned with the physical interpretation of results. It was suggested that assessing different scenarios based on coverage and initial IOU was more meaningful than evaluating the entire dataset. The study also explained the process of creating the dataset in detail, including the download procedure for GOES and VIIRS. The challenge of ensuring consistency between the initial GOES and VIIRS downloaded files regarding location, time, and projection was also explained. Additionally, the process of transforming VIIRS data from vector to raster format was explained in detail, making the framework more robust.

After evaluating the entire dataset, two observations were made. Firstly, the TBL model outperformed other models in terms of IOU. Secondly, the GLRMSE model showed an improvement in IPSNR (PSNR obtained by considering only true positive prediction) compared to the other models. However, these results may be biased towards the majority of sample types in the dataset. Further evaluation of categorized datasets (low coverage with high IOU (LCHI), low coverage with low IOU (LCLI), high coverage with high IOU (HCHI), and high coverage with low IOU (HCLI)) revealed the same patterns, except for the HCLI set where GLRMSE had a similar IOU score compared to the TBL model. However, analyzing multiple samples from each dataset type revealed that TBL model does not always produce the best results. The ranking of model performance in terms of IOU varied depending on the specific samples evaluated, highlighting the need for further improvement in evaluation metrics and the categorization of samples. Nonetheless, the GLRMSE model consistently predicted better radiance values of fire pixels, as indicated by its best IPSNR scores across all cases. Therefore, improving evaluation metrics and categorizing samples would enable the development of more reliable models.

The study's results offer a robust foundation for future research in creating high-resolution GOES images. To enhance the accuracy and applicability of the DL model, several directions for further studies can be pursued. First, while the proposed model can predict fire boundaries, there is room for improvement in actual radiance value prediction, which could be a focus of future research. Second, an adaptive region of interest (ROI) approach could be implemented to selectively include only relevant areas in the image. Currently, a constant value 'C' degree is used to determine the ROI's

corners, which is based on the biggest wildfire observed in the dataset available. This often results in smaller wildfires having a larger background area. Employing an adaptive ROI can decrease computational requirements and improve the model's speed. Third, incorporating more data for training, such as VIIRS data from NOAA-20 satellite, could increase the model's generalizability. Fourth, improving the rasterization process could enhance the model's accuracy by using more advanced techniques to align GOES and VIIRS data. Fifth, global normalization of VIIRS and GOES could help remove any biases introduced by variations in sensor properties and improve consistency between images. Sixth, adding a time component to the model could enable forecasting of changes in wildfire patterns and enhance the prediction’s accuracy. Finally, incorporating land use information, vegetation properties, and terrain data could improve wildfire pattern predictions. These potential enhancements represent future research directions in the field of high-resolution GOES image creation using DL models.

Bibliography

[1] "Wildfires and Acres | National Interagency Fire Center." https://www.nifc.gov/fire-information/statistics/wildfires (accessed Mar. 22, 2023).

[2] A. H. Taylor, L. B. Harris, and C. N. Skinner, "Severity patterns of the 2021 Dixie Fire exemplify the need to increase low-severity fire treatments in California's forests," *Environ. Res. Lett.*, vol. 17, no. 7, Jul. 2022, doi: 10.1088/1748-9326/AC7735.

[3] Y. Liao and C. Kousky, "The Fiscal Impacts of Wildfires on California Municipalities," *J. Assoc. Environ. Resour. Econ.*, vol. 9, no. 3, pp. 455–493, May 2022, doi: 10.1086/717492.

[4] A. L. Westerling, H. G. Hidalgo, D. R. Cayan, and T. W. Swetnam, "Warming and earlier spring increase Western U.S. forest wildfire activity," *Science (80-.).*, vol. 313, no. 5789, pp. 940–943, Aug. 2006, doi: 10.1126/SCIENCE.1128834/SUPPL_FILE/WESTERLING.SOM.PDF.

[5] D. M. Szpakowski and J. L. R. Jensen, "A Review of the Applications of Remote Sensing in Fire Ecology," *Remote Sens. 2019, Vol. 11, Page 2638*, vol. 11, no. 22, p. 2638, Nov. 2019, doi: 10.3390/RS11222638.

[6] P. Barmpoutis, P. Papaioannou, K. Dimitropoulos, and N. Grammalidis, "A review on early forest fire detection systems using optical remote sensing," *Sensors (Switzerland)*, vol. 20, no. 22, pp. 1–26, Nov. 2020, doi: 10.3390/S20226442.

[7] B. Pradhan, M. Dini, and H. Suliman, "Forest fire susceptibility and risk mapping using remote sensing and geographical information systems (GIS) Identification of rocks and their quartz content in Gua Musang gold field using Advanced Space-borne Thermal Emission and Reflection Radiometer (ASTER) imagery View project Semi-quantitative landslide risk assessment using GIS-based exposure analysis in Kuala Lumpur City View project", doi: 10.1108/09653560710758297.

[8] P. Barmpoutis, P. Papaioannou, K. Dimitropoulos, and N. Grammalidis, "A Review on Early Forest Fire Detection Systems Using Optical Remote Sensing," *Sensors 2020, Vol. 20, Page 6442*, vol. 20, no. 22, p. 6442, Nov. 2020, doi: 10.3390/S20226442.

[9] L. F. Radke *et al.*, "The wildfire experiment (WIFE): observations with airborne remote sensors," *Can. J. Remote Sens. 26(5) 406-417*, vol. 26, pp. 406–417, 2000, Accessed: Apr. 03, 2023. [Online]. Available: https://www.fs.usda.gov/research/treesearch/34726

[10] M. M. Valero and et. al., "On the use of compact thermal cameras for quantitative wildfire monitoring," *Adv. For. fire Res. 2018*, pp. 1077–1086, Nov. 2018, doi: 10.14195/978-989-26-16-506_119.

[11] A. Loew *et al.*, "Validation practices for satellite-based Earth observation data across communities," *Rev. Geophys.*, vol. 55, no. 3, pp. 779–817, Sep. 2017, doi: 10.1002/2017RG000562.

[12] L. B. Lentile *et al.*, "Remote sensing techniques to assess active fire characteristics and post-fire effects," *Int. J. Wildl. Fire. 15(3) 319--345.*, vol. 15, no. 3, pp. 319–345, 2006, doi: 10.1071/WF05097.

[13] J. Li, D. P. Roy, C. Atzberger, and G. Zhou, “A Global Analysis of Sentinel-2A, Sentinel-2B and Landsat-8 Data Revisit Intervals and Implications for Terrestrial Monitoring,” *Remote Sens. 2017, Vol. 9, Page 902*, vol. 9, no. 9, p. 902, Aug. 2017, doi: 10.3390/RS9090902.

[14] S. S. Kumar and D. P. Roy, “Global operational land imager Landsat-8 reflectance-based active fire detection algorithm,” *https://doi.org/10.1080/17538947.2017.1391341*, vol. 11, no. 2, pp. 154–178, Feb. 2017, doi: 10.1080/17538947.2017.1391341.

[15] X. Hu, Y. Ban, and A. Nascetti, “Sentinel-2 MSI data for active fire detection in major fire-prone biomes: A multi-criteria approach,” *Int. J. Appl. Earth Obs. Geoinf.*, vol. 101, p. 102347, Sep. 2021, doi: 10.1016/J.JAG.2021.102347.

[16] “Visible Infrared Imaging Radiometer Suite (VIIRS) - LAADS DAAC.” https://ladsweb.modaps.eosdis.nasa.gov/missions-and-measurements/viirs/ (accessed Feb. 09, 2023).

[17] L. Giglio, W. Schroeder, and C. O. Justice, “The collection 6 MODIS active fire detection algorithm and fire products,” *Remote Sens. Environ.*, vol. 178, pp. 31–41, Jun. 2016, doi: 10.1016/J.RSE.2016.02.054.

[18] W. Xu, M. J. Wooster, J. He, and T. Zhang, “First study of Sentinel-3 SLSTR active fire detection and FRP retrieval: Night-time algorithm enhancements and global intercomparison to MODIS and VIIRS AF products,” *Remote Sens. Environ.*, vol. 248, p. 111947, Oct. 2020, doi: 10.1016/J.RSE.2020.111947.

[19] P. Oliva and W. Schroeder, “Assessment of VIIRS 375 m active fire detection product for direct burned area mapping,” *Remote Sens. Environ.*, vol. 160, pp. 144–155, Apr. 2015, doi: 10.1016/J.RSE.2015.01.010.

[20] W. Schroeder *et al.*, “Validation of GOES and MODIS active fire detection products using ASTER and ETM+ data,” *Remote Sens. Environ.*, vol. 112, no. 5, pp. 2711–2726, May 2008, doi: 10.1016/J.RSE.2008.01.005.

[21] F. Li, X. Zhang, and S. Kondragunta, “Biomass Burning in Africa: An Investigation of Fire Radiative Power Missed by MODIS Using the 375 m VIIRS Active Fire Product,” *Remote Sens. 2020, Vol. 12, Page 1561*, vol. 12, no. 10, p. 1561, May 2020, doi: 10.3390/RS12101561.

[22] Y. Fu *et al.*, “Fire Detection and Fire Radiative Power in Forests and Low-Biomass Lands in Northeast Asia: MODIS versus VIIRS Fire Products,” *Remote Sens. 2020, Vol. 12, Page 2870*, vol. 12, no. 18, p. 2870, Sep. 2020, doi: 10.3390/RS12182870.

[23] A. Koltunov, S. L. Ustin, and E. M. Prins, “On timeliness and accuracy of wildfire detection by the GOES WF-ABBA algorithm over California during the 2006 fire season”, doi: 10.1016/j.rse.2012.09.001.

[24] F. Li, X. Zhang, S. Kondragunta, C. C. Schmidt, and C. D. Holmes, “A preliminary evaluation of GOES-16 active fire product using Landsat-8 and VIIRS active fire data, and ground-based prescribed fire records,” *Remote Sens. Environ.*, vol. 237, p. 111600, Feb. 2020, doi: 10.1016/J.RSE.2019.111600.

[25] M. Rashid, N. Sulaiman, M. Mustafa, S. Khatun, and B. S. Bari, “The classification of EEG signal using different machine learning techniques for BCI application,” *Commun. Comput. Inf. Sci.*, vol. 1015, pp. 207–221, 2019, doi:

10.1007/978-981-13-7780-8_17/COVER.
[26] S. Ren, Y. Zhou, and L. He, “Multi-object tracking with pre-classified detection,” *Adv. Intell. Syst. Comput.*, vol. 751, pp. 503–513, 2019, doi: 10.1007/978-3-319-78452-6_40/COVER.
[27] “Detection and Classification of Vehicle Types from Moving Backgrounds | SpringerLink.” https://link.springer.com/chapter/10.1007/978-3-319-78452-6_39 (accessed Mar. 05, 2023).
[28] M. Z. Nezhad, N. Sadati, K. Yang, D. Zhu, and M. Zafar Nezhad, “A Deep Active Survival Analysis Approach for Precision Treatment Recommendations: Application of Prostate Cancer,” 2018.
[29] Y. Xu, L. Wu, Z. Xie, and Z. Chen, “Building Extraction in Very High Resolution Remote Sensing Imagery Using Deep Learning and Guided Filters,” *Remote Sens. 2018, Vol. 10, Page 144*, vol. 10, no. 1, p. 144, Jan. 2018, doi: 10.3390/RS10010144.
[30] A. Albert, J. Kaur, and M. C. Gonzalez, “Using Convolutional Networks and Satellite Imagery to Identify Patterns in Urban Environments at a Large Scale,” *Proc. 23rd ACM SIGKDD Int. Conf. Knowl. Discov. Data Min.*, vol. Part F129685, pp. 1357–1366, Aug. 2017, doi: 10.1145/3097983.3098070.
[31] T. Oh, M. J. Chung, and H. Myung, “Accurate localization in urban environments using fault detection of GPS and multi-sensor fusion,” *Adv. Intell. Syst. Comput.*, vol. 447, pp. 43–53, 2017, doi: 10.1007/978-3-319-31293-4_4/COVER.
[32] N. T. Toan, P. Thanh Cong, N. Q. Viet Hung, and J. Jo, “A deep learning approach for early wildfire detection from hyperspectral satellite images,” *2019 7th Int. Conf. Robot Intell. Technol. Appl. RiTA 2019*, pp. 38–45, Nov. 2019, doi: 10.1109/RITAPP.2019.8932740.
[33] T. C. Phan, T. T. Nguyen, T. D. Hoang, Q. V. H. Nguyen, and J. Jo, “Multi-scale Bushfire Detection from Multi-modal Streams of Remote Sensing Data,” *IEEE Access*, 2020, doi: 10.1109/ACCESS.2020.3046649.
[34] Y. Zhao and Y. Ban, “GOES-R Time Series for Early Detection of Wildfires with Deep GRU-Network,” *Remote Sens.*, vol. 14, no. 17, Sep. 2022, doi: 10.3390/RS14174347.
[35] N. F. McCarthy, A. Tohidi, Y. Aziz, M. Dennie, M. M. Valero, and N. Hu, “A Deep Learning Approach to Downscale Geostationary Satellite Imagery for Decision Support in High Impact Wildfires,” *For. 2021, Vol. 12, Page 294*, vol. 12, no. 3, p. 294, Mar. 2021, doi: 10.3390/F12030294.
[36] “ABI │ GOES-R Series.” https://www.goes-r.gov/spacesegment/abi.html (accessed Oct. 04, 2022).
[37] “Products │ GOES-R Series.” https://www.goes-r.gov/products/overview.html (accessed Jan. 03, 2023).
[38] “GOES-R SERIES PRODUCT DEFINITION AND USERS’ GUIDE.” https://www.goes-r.gov/products/docs/PUG-L2+-vol5.pdf (accessed Oct. 23, 2022).
[39] “Data Products: Radiances | GOES-R Series.” https://www.goes-r.gov/products/baseline-radiances.html (accessed Jan. 03, 2023).
[40] M. D. Goldberg, H. Kilcoyne, H. Cikanek, and A. Mehta, “Joint Polar Satellite

System: The United States next generation civilian polar-orbiting environmental satellite system," *J. Geophys. Res. Atmos.*, vol. 118, no. 24, pp. 13,463-13,475, Dec. 2013, doi: 10.1002/2013JD020389.

[41] "Joint Polar Satellite System Exploring the Atmosphere." https://www.nasa.gov/sites/default/files/atoms/files/4._jpss_exploring_the_atmosphere_ppt.pdf (accessed Oct. 23, 2022).

[42] "How often is the MODIS/VIIRS satellite detection updated? - Deprecated Intterra Customer Support." https://intterra.helpdocs.com/faq/how-often-is-the-modisviirs-satellite-detection-updated (accessed Oct. 10, 2022).

[43] "Visible Infrared Imaging Radiometer Suite (VIIRS) | NESDIS." https://www.nesdis.noaa.gov/current-satellite-missions/currently-flying/joint-polar-satellite-system/jpss-mission-and-2 (accessed Oct. 18, 2022).

[44] "Visible Infrared Imaging Radiometer Suite (VIIRS) - LAADS DAAC." https://ladsweb.modaps.eosdis.nasa.gov/missions-and-measurements/viirs/ (accessed Jan. 04, 2023).

[45] "Visible Infrared Imaging Radiometer Suite (VIIRS) - LAADS DAAC." https://ladsweb.modaps.eosdis.nasa.gov/missions-and-measurements/viirs/ (accessed Oct. 07, 2022).

[46] "VNP14IMGTDL_NRT | Earthdata." https://www.earthdata.nasa.gov/learn/find-data/near-real-time/firms/vnp14imgtdlnrt (accessed Jan. 04, 2023).

[47] "VIIRS I-Band 375 m Active Fire Data | Earthdata." https://www.earthdata.nasa.gov/learn/find-data/near-real-time/firms/viirs-i-band-375-m-active-fire-data (accessed Oct. 04, 2022).

[48] "Satellite (MODIS) Thermal Hotspots and Fire Activity - Overview." https://www.arcgis.com/home/item.html?id=b8f4033069f141729ffb298b7418b653 (accessed Nov. 25, 2022).

[49] "Moderate Resolution Imaging Spectroradiometer (MODIS) - LAADS DAAC." https://ladsweb.modaps.eosdis.nasa.gov/missions-and-measurements/modis/ (accessed Oct. 23, 2022).

[50] "GOES-16/17/18 on Amazon Download Page." https://home.chpc.utah.edu/~u0553130/Brian_Blaylock/cgi-bin/goes16_download.cgi?source=aws&satellite=noaa-goes17&domain=C&product=ABI-L2-CMIP&date=2020-09-09&hour=4 (accessed Jan. 04, 2023).

[51] "NASA | LANCE | FIRMS." https://firms.modaps.eosdis.nasa.gov/country/ (accessed Oct. 07, 2022).

[52] "LAND, ATMOSPHERE NEAR REAL-TIME CAPABILITY FOR EOS (LANCE) | Earthdata." https://www.earthdata.nasa.gov/learn/find-data/near-real-time/lance (accessed Oct. 09, 2022).

[53] "Raster vs. vector: What are the differences? | Adobe." https://www.adobe.com/creativecloud/file-types/image/comparison/raster-vs-vector.html (accessed Mar. 09, 2023).

[54] "CAL FIRE." https://www.fire.ca.gov/ (accessed Mar. 01, 2023).

[55] "2020 Western United States Wildfires - Homeland Security Digital Library." https://www.hsdl.org/c/tl/2020-wildfires/ (accessed Mar. 01, 2023).

[56] “GOES-17 ABI Performance │ GOES-R Series.” https://www.goes-r.gov/users/GOES-17-ABI-Performance.html (accessed Mar. 01, 2023).
[57] “STAR - Aerosol, Fire, and Trace Gases Training - GOES Imager Projection.” https://www.star.nesdis.noaa.gov/atmospheric-composition-training/satellite_data_goes_imager_projection.php (accessed Mar. 04, 2023).
[58] “Resampling — Satpy 0.37.2.dev0+g905943c2.d20220815 documentation.” https://satpy.readthedocs.io/en/stable/resample.html?highlight=areadefination (accessed Oct. 23, 2022).
[59] “satpy.scene module — Satpy 0.37.2.dev0+g905943c2.d20220815 documentation.” https://satpy.readthedocs.io/en/stable/api/satpy.scene.html (accessed Oct. 23, 2022).
[60] “WGS 84 - WGS84 - World Geodetic System 1984, used in GPS - EPSG:4326.” https://epsg.io/4326 (accessed Feb. 09, 2023).
[61] “Satpy’s Documentation — Satpy 0.37.2.dev0+g905943c2.d20220815 documentation.” https://satpy.readthedocs.io/en/stable/ (accessed Oct. 23, 2022).
[62] “Rasterization: a Practical Implementation.” https://www.scratchapixel.com/lessons/3d-basic-rendering/rasterization-practical-implementation/rasterization-stage.html (accessed Mar. 07, 2023).
[63] “What is Rasterization? - Definition from Techopedia.” https://www.techopedia.com/definition/13169/rasterization (accessed Jan. 05, 2023).
[64] “pyproj 3.4.0 documentation.” https://pyproj4.github.io/pyproj/stable/ (accessed Oct. 23, 2022).
[65] “scipy.interpolate.NearestNDInterpolator — SciPy v1.10.0 Manual.” https://docs.scipy.org/doc/scipy/reference/generated/scipy.interpolate.NearestNDInterpolator.html (accessed Feb. 09, 2023).
[66] “GDAL — GDAL documentation.” https://gdal.org/ (accessed Oct. 23, 2022).
[67] S. Park, H. M. Gach, S. Kim, S. J. Lee, and Y. Motai, “Autoencoder-Inspired Convolutional Network-Based Super-Resolution Method in MRI,” *IEEE J. Transl. Eng. Heal. Med.*, vol. 9, 2021, doi: 10.1109/JTEHM.2021.3076152.
[68] W. Wang, Y. Huang, Y. Wang, and L. Wang, “Generalized autoencoder: A neural network framework for dimensionality reduction,” *IEEE Comput. Soc. Conf. Comput. Vis. Pattern Recognit. Work.*, pp. 496–503, Sep. 2014, doi: 10.1109/CVPRW.2014.79.
[69] S. Albawi, T. A. Mohammed, and S. Al-Zawi, “Understanding of a convolutional neural network,” *Proc. 2017 Int. Conf. Eng. Technol. ICET 2017*, vol. 2018-January, pp. 1–6, Mar. 2018, doi: 10.1109/ICENGTECHNOL.2017.8308186.
[70] W. Shi *et al.*, “Is the deconvolution layer the same as a convolutional layer?,” Sep. 2016, doi: 10.48550/arxiv.1609.07009.
[71] H. T. Chiang, Y. Y. Hsieh, S. W. Fu, K. H. Hung, Y. Tsao, and S. Y. Chien, “Noise Reduction in ECG Signals Using Fully Convolutional Denoising Autoencoders,” *IEEE Access*, vol. 7, pp. 60806–60813, 2019, doi: 10.1109/ACCESS.2019.2912036.
[72] O. J. D. Barrowclough, G. Muntingh, V. Nainamalai, and I. Stangeby, “Binary segmentation of medical images using implicit spline representations and deep

learning," *Comput. Aided Geom. Des.*, vol. 85, Feb. 2021, doi: 10.1016/j.cagd.2021.101972.

[73] D. Duque-Arias *et al.*, "On power Jaccard losses for semantic segmentation," Feb. 2021, Accessed: Feb. 13, 2023. [Online]. Available: https://hal.science/hal-03139997

[74] S. Narayan, "The generalized sigmoid activation function: Competitive supervised learning," *Inf. Sci. (Ny).*, vol. 99, no. 1–2, pp. 69–82, Jun. 1997, doi: 10.1016/S0020-0255(96)00200-9.

[75] Z. Jun and H. Jinglu, "Image segmentation based on 2D Otsu method with histogram analysis," *Proc. - Int. Conf. Comput. Sci. Softw. Eng. CSSE 2008*, vol. 6, pp. 105–108, 2008, doi: 10.1109/CSSE.2008.206.

[76] "Weights & Biases – Developer tools for ML." https://wandb.ai/site (accessed Mar. 15, 2023).

[77] D. P. Kingma and J. L. Ba, "Adam: A Method for Stochastic Optimization," *3rd Int. Conf. Learn. Represent. ICLR 2015 - Conf. Track Proc.*, Dec. 2014, doi: 10.48550/arxiv.1412.6980.

[78] K. You, M. Long, J. Wang, and M. I. Jordan, "How Does Learning Rate Decay Help Modern Neural Networks?," Aug. 2019, Accessed: Apr. 03, 2023. [Online]. Available: https://arxiv.org/abs/1908.01878v2

[79] "PyTorch." https://pytorch.org/ (accessed Feb. 25, 2023).

[80] Lareau, N. P., Donohoe, A., Roberts, M., & Ebrahimian, H. (2022). "Tracking wildfires with weather radars". *Journal of Geophysical Research: Atmospheres,* 127, e2021JD036158. https://doi.org/10.1029/2021JD036158

Appendix

Appendix A

Wildfire events used for this study

Site	Central Longitude	Central Latitude	Fire Start date	Fire End date
Kincade	-122.780	38.792	2019-10-23	2019-11-06
Walker	-120.669	40.053	2019-09-04	2019-09-25
Tucker	-121.243	41.726	2019-07-28	2019-08-15
Taboose	-118.345	37.034	2019-09-04	2019-11-21
Maria	-118.997	34.302	2019-10-31	2019-11-05
Redbank	-122.64	40.12	2019-09-05	2019-09-13
Saddle ridge	-118.481	34.329	2019-10-10	2019-10-31
Lone	-121.576	39.434	2019-09-05	2019-09-13
Chuckegg creek fire	-117.42	58.38	2019-05-15	2019-05-22
Eagle bluff fire	-119.5	49.42	2019-08-05	2019-08-10
Richter creek fire	-119.66	49.04	2019-05-13	2019-05-20
LNU lighting complex	-122.237	38.593	2020-08-18	2020-09-30
SCU lighting complex	-121.438	37.352	2020-08-14	2020-10-01
CZU lighting complex	-122.280	37.097	2020-08-16	2020-09-22
August complex	-122.97	39.868	2020-08-17	2020-09-23
North complex fire	-120.12	39.69	2020-08-14	2020-12-03
Glass fire	-122.496	38.565	2020-09-27	2020-10-30
Beachie wildfire	-122.138	44.745	2020-09-02	2020-09-14
Beachie wildfire 2	-122.239	45.102	2020-09-02	2020-09-14
Holiday farm wildfire	-122.49	44.15	2020-09-07	2020-09-14
Cold spring fire	-119.572	48.850	2020-09-06	2020-09-14
Creek fire	-119.3	37.2	2020-09-05	2020-09-10
Blue ridge fire	-117.68	33.88	2020-10-26	2020-10-30
Silverado fire	-117.66	33.74	2020-10-26	2020-10-27
Chuckegg creek fire	-117.42	58.38	2019-05-15	2019-05-22
Bond fire	-117.67	33.74	2020-12-02	2020-12-07
Washinton fire	-119.556	48.825	2020-08-18	2020-08-30
Oregon fire	-121.645	44.738	2020-08-17	2020-08-30
Talbott creek	-117.01	49.85	2020-08-17	2020-08-30
Christie mountain	-119.54	49.364	2020-08-18	2020-09-30
Bush fire	-111.564	33.629	2020-06-13	2020-07-06
Magnum fire	-112.34	36.61	2020-06-08	2020-07-06
Bighorn fire	-111.03	32.53	2020-06-06	2020-07-23

Santiam fire	-122.19	44.82	2020-08-31	2020-09-30
Holiday farm fire	-122.45	44.15	2020-09-07	2020-09-30
Slater fire	-123.38	41.77	2020-09-07	2020-09-30
Eagle bluff fire	-119.5	49.42	2019-08-05	2019-08-10
Alberta fire 1	-118.069	55.137	2020-06-18	2020-06-30
Doctor creek fire	-116.09788	50.0911	2020-08-18	2020-08-24
Magee fire	-123.22	49.88	2020-04-15	2020-04-16
Pinnacle fire	-110.201	32.865	2021-06-10	2021-07-16
Backbone fire	-111.677	34.344	2021-06-16	2021-07-19
Rafael fire	-112.162	34.942	2021-06-18	2021-07-15
Telegraph fire	-111.092	33.209	2021-06-04	2021-07-03
Dixie	-121	40	2021-06-15	2021-08-15
Monument	-123.33	40.752	2021-07-30	2021-10-25
River complex	-123.018	41.143	2021-07-30	2021-10-25
Antelope	-121.919	41.521	2021-08-01	2021-10-15
Mcfarland	-123.034	40.35	2021-07-29	2021-09-16
Beckwourth complex	-118.811	36.567	2021-07-03	2021-09-22
Windy	-118.631	36.047	2021-09-09	2021-11-15
Mccash	-123.404	41.564	2021-07-31	2021-10-27
Knpcomplex	-118.811	36.567	2021-09-10	2021-12-16
Tamarack	-119.857	38.628	2021-07-04	2021-10-08
French	-118.55	35.687	2021-08-18	2021-10-19
Lava	-122.329	41.459	2021-06-25	2021-09-03
Alisal	-120.131	34.517	2021-10-11	2021-11-16
Salt	-122.336	40.849	2021-06-30	2021-07-19
Tennant	-122.039	41.665	2021-06-28	2021-07-12
Bootleg	-121.421	42.616	2021-07-06	2021-08-14
Cougar peak	-120.613	42.277	2021-09-07	2021-10-21
Devil'sKnob Complex	-123.268	41.915	2021-08-03	2021-10-19
Roughpatch complex	-122.676	43.511	2021-07-29	2021-11-29
Middlefork complex	-122.409	43.869	2021-07-29	2021-12-13
Bull complex	-122.009	44.879	2021-08-02	2021-11-19
Jack	-122.686	43.322	2021-07-05	2021-11-29
Elbowcreek	-117.619	45.867	2021-07-15	2021-09-24
Blackbutte	-118.326	44.093	2021-08-03	2021-09-27
Fox complex	-120.599	42.21	2021-08-13	2021-09-01
Joseph canyon	-117.081	45.989	2021-06-04	2021-07-15
Wrentham market	-121.006	45.49	2021-06-29	2021-07-03
S-503	-121.476	45.087	2021-06-18	2021-08-18

Grandview	-121.4	44.466	2021-07-11	2021-07-25
Lickcreek fire	-117.416	46.262	2021-07-07	2021-08-14
Richter mountain fire	-119.7	49.06	2019-07-26	2019-07-30